Monolithic Interferometer in twin optical fibers

Study to build an all-in fiber Mach-Zenhder interferometer in twin optical fibers

ANTOINE LORIETTE

Supervisor: Walter Margulis
Examiner: Lars-Gunnar Andersson

TRITA FYS 2007-90 ISSN 0280-316X ISRN KTH/FYS/–07:90–SE

Abstract

Over the last few years, Acreo has led research activities in the area of special optical fibers, thanks to its facility in Hudiskvall.

One of the fibers fabricated consists of a double fiber, each half made of the same fiber and connected to the other half by glass during the drawing. This double-fiber opens the possibility of creating and controlling two similar optical paths in the same fiber.

This characteristic is directly related to the present diploma work, which investigates the feasibility of creating stable and balanced fiber interferometers in an easy and cost-effective way.

The first step has been to find a method to access the fiber halves individually and provide low-loss connections towards pigtails within a reproductive procedure.

Their characterization through the measure of their Polarization Dependant Loss and Differential Group Delay has been the second step. It allows to compare and quantify the quality of the double fiber against the standard telecom fiber in the market.

The realization of optical components requires the control of complex tasks such as Coupler fabrication and Fiber Bragg grating inscription.

Both activities have been realized in the double-fiber. They are presented successively, with their respective results.

Finally, a Michelson interferometer is presented. The measurements and results presented give valuable information about the possibilities offered by the double-fiber geometry.

Eventually, an additional fiber component is presented. It deals with the realization of a monolithical Fabry-Perot interferometer into a capillary fiber.

Acknowledgments

During this diploma work, I had the pleasure of meeting many nice people. I would like to thank them for their contribution and the very useful support they have shown to my work.

My first acknowledgment is dedicated to my supervisor, *Walter Margulis*, whose thrust and backing have been an important reason of my motivation and faith in the project. He continuously came with new ideas to solve the problems I experienced, and his buoyancy and never ending optimism contributed to create the cheerful but productive atmosphere that surrounded my work in Acreo.

The team of the Fiber Component Lab, of which I belonged to, has also been of a very precious help for its transfer of training.

Sacha Petrovenko contributed to my formation concerning various techniques used in the lab.

Erik Petrini took part in the project when it was dealing with Fiber Bragg Grating inscription. I thank him for his help, but also for having shared a lots of funny swedish stories.

I would like to thank *Leif Kellberg* for his daily help with the equipment, and *Erik Setterlund* for his advises. I wish him also a lot of success for the ongoing work on the Paso Doble.

I thank *Suzanne Lacroix* for her extremely valuable tips on coupler fabrication.

The universities of ULP and KTH, and their respective teachers, have been the grounds for this diploma work. I would like to thank *Göran Manneberg* for having recommended me this diploma work, *Jelila Labed* and *Eric Fogarassy* for having make my stay in Sweden a reality.

ACREO AB

The present work was carried out at Acreo [6]. It is located in the Stockholm's science district, in the city of Kista. Acreo is an R&D company with main objective to refine and transfer research results into industrially viable products and processes in the fields of electronics and optics.

Acreo carries out market oriented applied R&D, consultancy and small-scall production. It was founded to provide a bridge between the Universities and the Industry.

Acreo is organized in seven technology departments. These departments are active in the fields of Imaging, Photonics, Interconnect and Packaging, Silicon Carbide Electronics, Micro Systems Technology, Surface Characterization and System Level Integration. The department of Business Services is dedicated to technology transfer and support for small and medium-sized companies.

Acreo is owned jointly by an industrial association, FMOF and the state-owned holding company IRECO. Today there are 140 employees of which 90 have an academic degree.

The present work took place within the department of Photonics, which has some 30 members. The laboratories include a complete fiber fabrication facility devoted to the manufacture of special fibers, clean room facilities for the manufactures of advanced III-V semiconductor structures, a laser laboratory with numerous high-power systems, and an advanced fiber grating fabrication facility.

The main research lines developed at the fiber components group make use of special fibers fabricated at Fiberlab in Hudiksvall. They include special fiber Bragg grating, high-temperature resistant fiber Bragg grating, internal electrode fibers, electrooptcical fibers, microcells and fiber sensors.

Chapter 1

Introduction

As the name of the thesis describes it, the subject is mainly about interferometers[1].

In optics, an interferometer is an instrument that uses for different purpose the phenomenon of interference, so to say the superposition or algebraic sum of two waves. The necessity of having several coherent waves has led from the beginning to the use of one light source associated with various splitting devices.

In the experience of Young, close-lying illuminated holes in a plane are use to create the needed two coherent light sources. With the interferometers of Michelson and Mach-Zehnder the optical beam splitter is used. The remarkable precision of

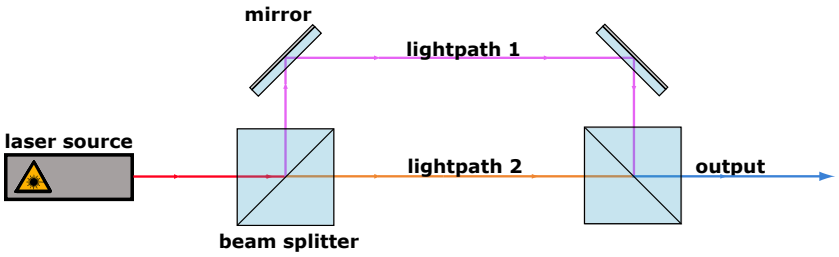

Figure 1.1: Mach-Zehnder interferometer in free-space. The first beam splitter creates an additional lightpath (in purple) that interferes with the straight path (in orange) after the second beam splitter.

those setups, in the order of the wavelength, is a reason of their early success. In 1887, the Michelson interferometer used in the Michelson-Morley experiment[2] led to the first strong evidence against the theory of a luminiferous aether. Nowadays, it is used in schools to introduce the interference phenomenon, or in the research and industry as a high precision sensor.

With the advent and deployment of optical networks, interferometers have been build into optical fibers, where directional couplers play the role of beam splitters.

The Mach-Zehnder interferometer[2] consists here the ground setup to perform

[1] Most of the basis on general Optics can be found in the book of Hecht[1].

[2] later on abbreviated to *MZI*

many interesting functions, among which an electrically driven optical switch and an Add/Drop multiplexer[3].

In optical networks, optical switches assume a central role, for example in the provision of lightpaths into optical crossconnects or to perform packet switching. Optical switches and amplitude modulators find also other applications, for instance in sensing and in the control of laser sources.

However, meoms or external polarization effect based setups (Pockels cell for Q-switching) are usually preferred to perform those functions.

Furthermore, the Wavelength Division Multiplexing extensively used in optical networks gives a special role to the *ADM*, as it is the case for the Erbium doped fiber amplifier where a multiplexer is used to separate the signal from the source. In this particular case, a simple coupler can be used[3].

A *MZI* structure may lead to such efficient and complex task, but is still complicated to implement monolithically. In this thesis we propose thus to investigate the feasibility of those concept through the use of new atypical fibers.

Two simple setups can then be presented.

The optical switch studied consists of a fully equilibrated *MZI* in which one of the arms can be used to induce a π-shift[4, 5] to the light traveling through. The output will then be switched on command from one arm to the other, fig.1.2.

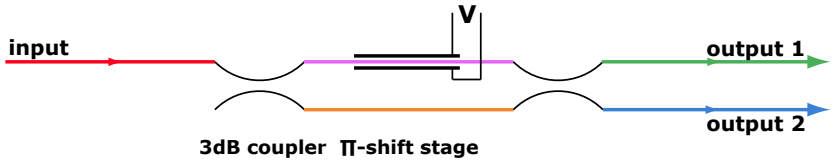

Figure 1.2: Optical switch setup based on a Mach-Zehnder interferometer and voltage controlled phase shifting stage embedded in a fiber with holes. The $-3dB$ coupler is the in-fiber counterpart to the open-air beam splitter.

The *ADM* is designed in a equilibrated *MZI* in which both arms include a *FBG*. With this configuration, the input signal contains all wavelengths, the drop port contains the dropped wavelength from the input signal, while the add port allows to re-inject this wavelength into the output port that will contain again the full spectrum, fig.1.3.

Despite its simple scheme, an equilibrated *MZI* structure is still difficult to obtain experimentally since it needs a perfect arm's length match. When based on two industrial couplers linked by independent standard telecom fibers, it encounters two main problems.

The first one is to realize the 4 splices of the arms between the couplers and obtain the exact same length. For example, a $1mm$ mismatch at $1550\mu m$ gives a bandwidth of $1.64nm$[4], to be compared with the $40nm$ of the C-band.

[3] later on abbreviated to *ADM*

[4] The bandwidth at λ is defined by $\delta\lambda = \frac{\lambda^2}{n \cdot \delta L}$, and δL is the length mismatch.

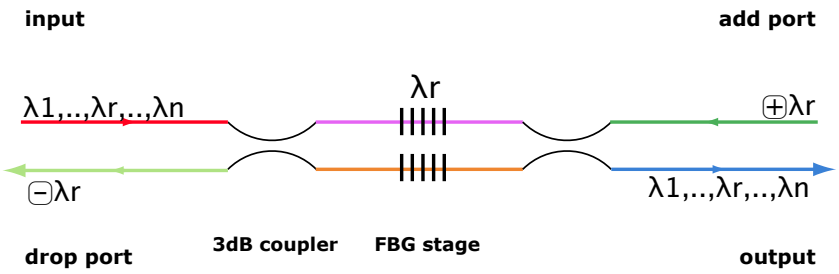

Figure 1.3: Add/Drop multiplexer setup based on a Mach-Zehnder interferometer and two equivalent wavelength selective *FBG* written in both arm.

The second problem comes form the external accoustic and thermal perturbations. They reduce the overall stability by randomly influencing the differential light path between the both arms. The performance are then highly dependent of time and temperature.

To overcome those problems, Acreo thought about a new type of fiber that may sidestep those difficulties.

Chapter 2

Atypical optical fibers

Acreo's double fibers have constituted the grounds of the thesis in Acreo. Their main characteristic is to be composed of two identical halves, each one similar to a standard telecom fiber[1], both halves connected by a narrow silica glass bridge along the length. This section will described how they are made and their overall geometry, see fig.E.1 and fig.E.2 - p.79.

2.1 Fabrication of the fibers

The fibers are made in Acreo's facility in Hudiksvall, where an up-to-date fiber fabrication laboratory is available.

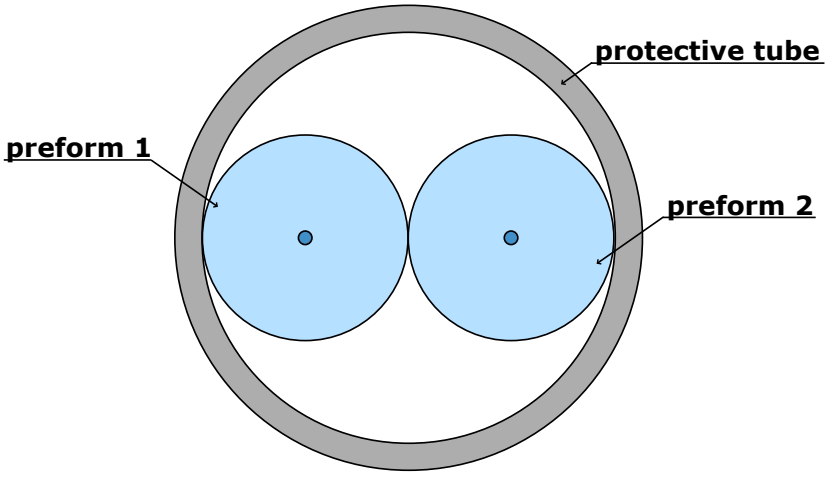

Figure 2.1: Preform setup for *PaDo*. The protective tube holds both preforms in place, before their lower parts are melt together.

[1] later on abbreviated to *STF*

The technique used to make double fibers is rather similar to the one used for *STF*. However, instead of melting one preform at a time, two identical preforms stuck together at their extreme by a glass protective tube are melted simultaneously, fig.2.1. At the temperature of 1800℃, the glass becomes soft and the capillarity forces lead to the reunion in the middle of the two fibers, fig.2.5(a).

The double fibers have also been made with holes inside, in the same fashion as the single fibers with holes. In that case, the holes are made with diamond coated drilling machines, fig.2.2.

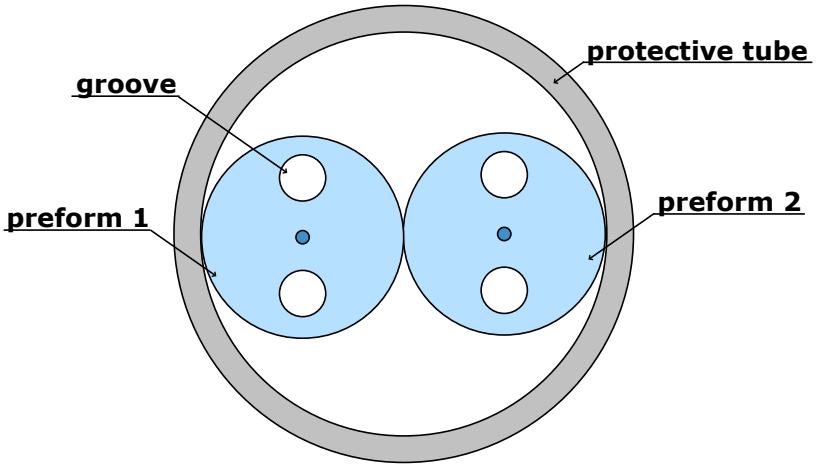

Figure 2.2: Preform setup for *PaDowH*

Once heated and pulled, the geometry is conserved, fig.2.5(b). A higher atmospheric pressure is applied in the holes during the process to prevent them from collapsing.

2.2 Advantages of the geometry

The fibers have been observed and measured with a microscope to characterized their outer geometry, as depicted in fig.2.3 and fig.2.4.

The first fiber is called *Paso Doble*, that will be abbreviate to *PaDo*. It is composed by two $125\mu m$ *STF* glued together by a $5\mu m$ thick piece of glass.

In order to build a *MZI*, the advantages of this fiber are multiple. Directional coupler can be fabricated using the technic of melting and pulling[7, 8, 9, 10] with this geometry, since the relative position of the fiber halves is fixed by the glass bridge. Moreover, a matched optical length of the two arms between the couplers will be insured if the halves of the fiber have equal propagation constant. Finally, the stability with regards to acoustic [2] and thermal perturbation will be increased

[2]The transversal stress in the vertical direction will have the same effect in both fibers.

since the two core are part of the same piece of glass and distant from only $130\mu m$.

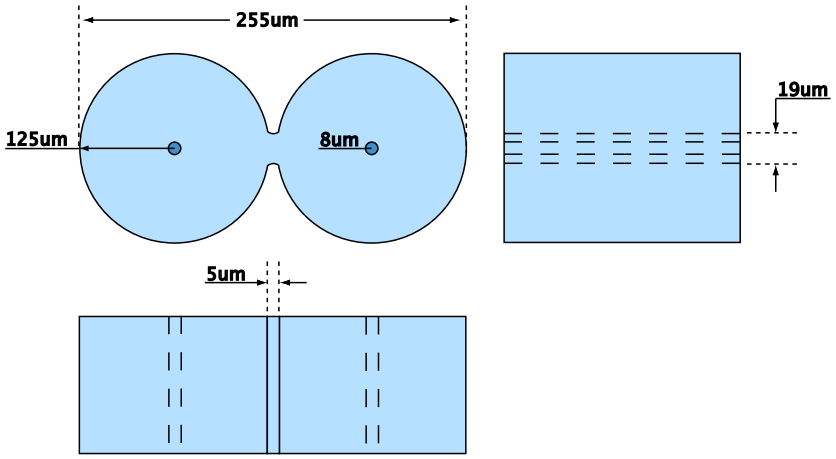

Figure 2.3: Dimensions of *PaDo*

The second fiber is called *Paso Doble with Holes*[3] named in reference to *PaDo*. The longitudinal symmetry is similar to *PaDo*, but *PaDowH* is composed of two identical fibers with $24\mu m$ holes,fig.2.4. Due to manufacturing matters, it exhibits an additional twist in the disposition of the holes, and small excentricity of the outer diameter.

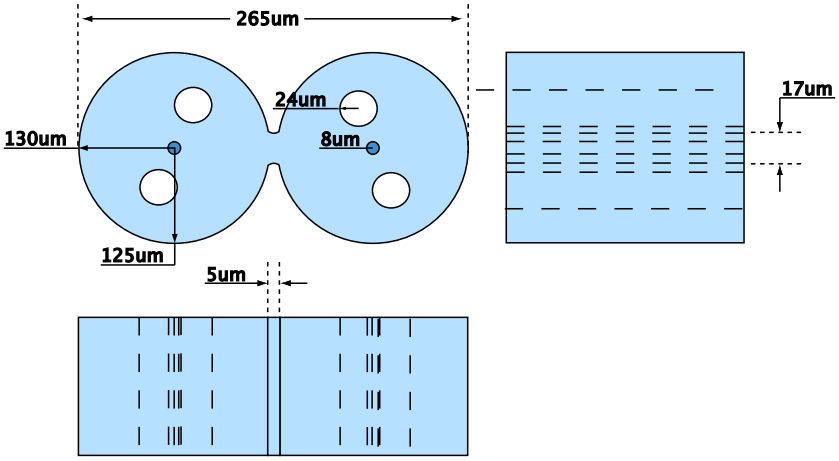

Figure 2.4: Dimensions of *PaDowH*

Fibers with holes have shown themselves very useful in the field of optics, mainly as pressure sensors[11] as they were invented for, but have also been used lately on the opposite way. The idea is to fill the holes with internal electrodes that apply

[3]later on abbreviated to *PaDowH*

a stress on the core when driven by a current. This stress induces a controllable phase shift[5] to the light traveling through the fiber.

This new geometry may suppress some restrictions encountered by the use of *STF*. But because it breaks the rotational symmetry, which is usually a constant in the Fiber Optics field, the handling of *PaDo* and *PaDowH* will require additional care.

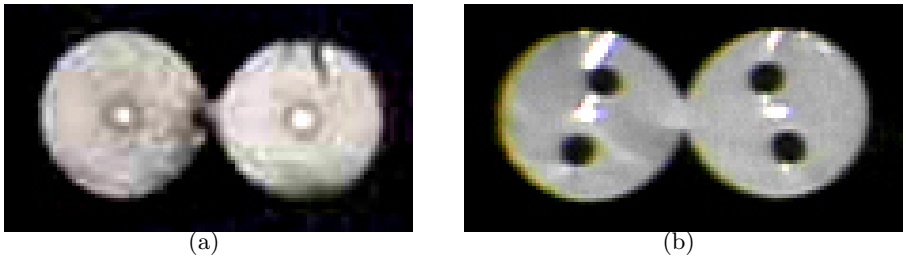

(a) (b)

Figure 2.5: *PaDo*(a) and *PaDowH*(b) seen under an optical microscope, see also fig.E.1 and fig.E.2 - p.79.

Chapter 3

Building a setup - making connections

This chapter explains the steps needed to build a setup with those double fibers. The main goal is to achieve the connection of the four ports of a *PaDo* or *PaDowH* to four other pigtails with low insertion losses through a reproducible process.

3.1 Accessing the fibers

As with *STF* the first step is to remove the acrylate coating. It is not possible to strip it with the regular mechanical tool that has a circular section, but the solution of using dichloromethane(DCM) to dissolve the acrylate works well.

The fiber's coating is weakened by a soft sandpaper, before being immersed in a becher containing the *DCM* during approximately 30 secondes. The coating is at that point weakened enough to be removed manually with some lens paper.

In the case of *PaDowH* it is possible to close the holes with nail vanish to prevent the *DCM* to enter. Although this step is not compulsory since *DCM* is highly volatile and has a tendency to flow out of the holes.

The bare fibers are then accessible.

3.2 Separation of the arms

Accessing the arms individually is compulsory[1] to realize the splicing process. *PaDo* and *PaDowH* are then etched to dissolve the piece of glass linking the two arms.

A solution of Hydrofluoric acid(HF) concentrated at 40% is used. The speed of etching is approximately of $0.9\mu m/min$, so that according to fig.2.3 and fig.2.4 the expected time to separate the fibers is approximately of 11 minutes for the case of *PaDo* and 10 minutes for *PaDowH*.

Actually, the experiments show that 18 minutes and 15 minutes are mandatory for, respectively, *PaDo* and *PaDowH*. After this step, the two arms are fully sep-

[1]Direct double splicing is really difficult to perform since the fibers have to be aligned in translation and in rotation. As a result, the obtained average insertion loss had a value around $10dB$. Later work from Erik Setterlund will cut down this loss to $1dB$.

arated, and it is then possible to work on one without affecting the other. The obtained setup etched over 15 cm shows this typical shape, fig.3.1.

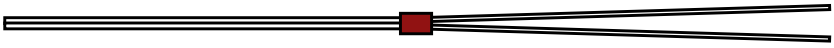

Figure 3.1: *PaDo* arms separated and strengthen with nail vanish.

However, after looking at the fibers under a microscope, it appears that their outer geometry is not round anymore. The rotational symmetry is broken a second time. Furthermore, by injecting light into the fiber, the core shows an eccentric position, fig.3.2(a).

Those two points are critical for the quality of the splice. First, a tension of surface can be brought on when the fibers are connected together, and second, a small misalignment of the cores gives rise to a significant insertion loss.

To overcome these problems, a longer etching process has been investigated. Unfortunately, even after 50 minutes, the non-round geometry appears to be still present, see fig.3.2(b).

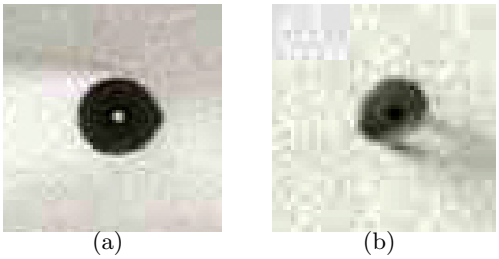

(a) (b)

Figure 3.2: *PaDo* etched 18 minutes (a), *PaDo* etched 50 minutes (b). The remaining of the glass bridge is noticeable on the right in figure (a), as is the eccentricity of the core.

Eventually, the process where the etching time is reduced to its minimum is chosen in order to maximize the external size of the fiber, and therefor preserve as much as possible its mechanical resistance.

3.3 Taping the arms

Because of the geometry of the cleaving and splicing machines, the arms needs to be separate one from another. It must be possible to insert them individually into those machines.

The physical separation and taping of the arms is critical since the setup is at that point very fragile. To reinforce the weakest point, where the fibers separate, some nail vanish or UV curing glue is applied and dried, fig.3.1. It is possible to

recognize that point by spotting the discontinuity in the reflection of incident light over the cladding it produces.

The arms are then bent away from each other and taped at separated positions. By applying a gentle force, it is possible to create an angle of 45°-90° between them, see fig.3.3.

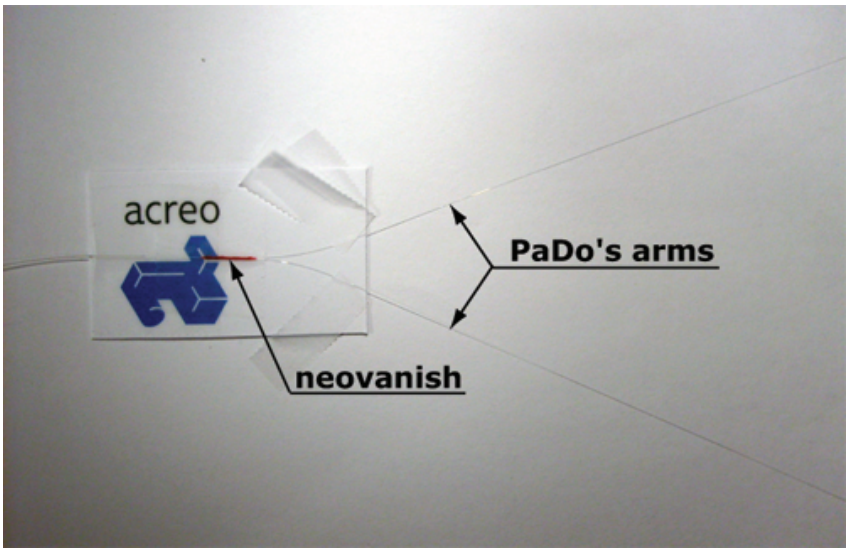

Figure 3.3: *PaDo* taped on a cardboard ready to be cleaved and spliced.

The setup is now ready for the cleaving and splicing process.

3.4 Cleaving the arms

The cleaving process is somehow similar with the one use for *STF* but a special care must be made when aligning the fiber into the cleaver.

Because of its eccentricity and relative thinness, a slight twist in the alignment produces a major angle a the very tip of the fiber.

The splicing machine (model *FSU 975 PM-A*) used during the project included an angle measurement system[2] that allows to measure the alignment angle (α) and gap angle (β) of *STF* with the one of *PaDo*. The value of the cleaving angle γ is obtained with the relation : $\gamma = \beta - \alpha$.

The *PaDo* is invariably placed on the left, while connected to a *STF* on the right. We obtain the following values after 71 attempts, tbl.3.1. The value with the superscript $_{left}$, resp. $_{right}$ are thus for *PaDo*, resp. *STF*.

First, the *PaDo* shows better result than the *STF* concerning its alignment into the fiber holders. The average view angle is decreased by 30% and exhibit a standard deviation 31% lower than *STF*.

[2]The data taken from the measurement is displayed in tbl.B.4, p.72.

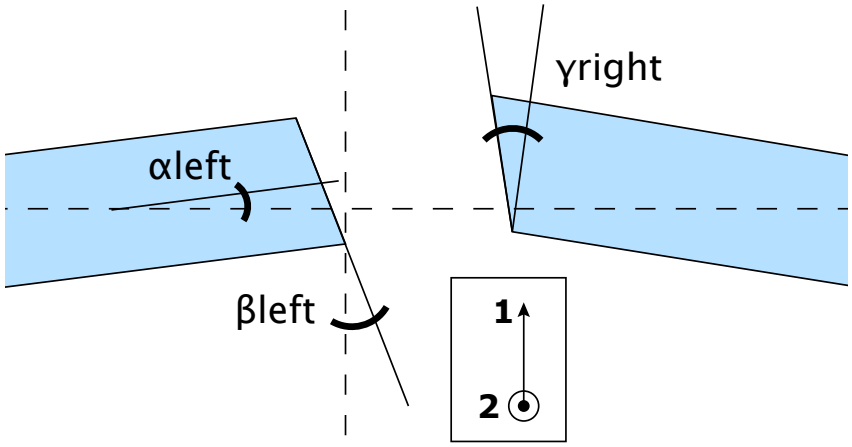

Figure 3.4: Definition of the measured angles in the splicer, α, β and γ. The camera axis are represented by the vectors 1 and 2, and the angle of sight is collinear to 1.

	α_{left}	β_{left}	γ_{left}	α_{right}	β_{right}	γ_{right}
avg	0.35	1.63	1.28	-0.5	0.72	1.23
stdev	0.20	1.21	1.23	0.26	0.55	0.58

Table 3.1: Measured value of the cleaving angles for *STF* on the left and *PaDo*on the right. The unit is the degree.

Second, the figures shows as expected that a cleave on *PaDo* is more likely to exhibit an angle at the fiber tip. Even if the difference is only of 4% in average, the standard deviation is more than two times greater. Since the value of the cleave angle is critical for the quality of the splice, a too large value led the fiber to be cleaved again.

3.5 Splicing the arms

So far, three techniques have been investigated to splice the *PaDo* and the *PaDowH*with *STF* using two different splicers.

3.5.1 Splicing machines

The first splicer that has been used is a fusion splicer *FSU 925 RTC* from *Ericsson*. Although it is a basic splicer, it include several program adapted to different fibers, classic fiber holders and a Real Time Control(*RTC*) splicing procedure to splice fibers that have a bad concentricity.

The second splicer is an evolved version of the previous splicer. The model is *FSU 975 PM-A* from *Ericsson*. The basics features are the same, but the number of parameters for the splicing process is increased.

In addition, it includes the former angle measurement system, and some pre-programmed splicing procedure for different kind of fibers (Erbium doped fiber, depressed cladding fiber, ...) or to realize fibers components (taper or microlense). The fibers holders are free in rotation, and are mounted with a vacuum pump. It is thus possible to rotate the fiber at adjustable angles within 360ř.

3.5.2 Method n°1 - *FSU 925 RTC* with cladding alignment

The first method used the *FSU 925 RTC* with the program made for *STF*, so to say with cladding alignment. It exhibited some good results for the insertion loss, and a success rate of the process equal to 100%, tbl.3.2.

min	max	avg	stdev	success
0.36	6.21	1.71	2.12	100%

Table 3.2: Splicing method n°1 - Insertion loss [dB]

However, a $6dB$ insertion loss obtained on one arm of a setup revealed the presence of the eccentrically positioned core, as mentioned in section 3.2, p.9.

The alignment procedure is based on the picture taken by the two orthogonal cameras 1&2, fig.3.5. Using this method leads invariably to a mismatch between the core of the *STF* and the *PaDo* included in an interval $[0; d]$, where d is the eccentricity.

A quick analysis of fig.3.2(a) gives a value for d included in $[0; 5\mu m]$, which compared to the size of the core ($10\mu m$) gives at maximum a mismatch of around 50%. Such a mismatch is responsible for the maximum value of the measured insertion losses in table 3.2.

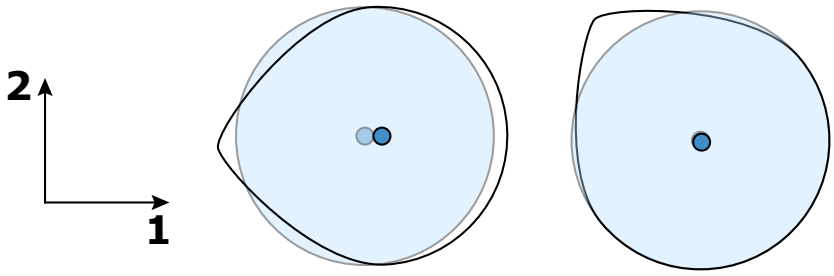

Figure 3.5: Core mismatch for 2 positions with perfect cladding shape alignment. The splicing machine is in these case unable to detect the core alignment mismatch.

3.5.3 Method n°2 - *FSU 975 PM-A* with Real Time Control (*RTC*)

The second splicer has then been choosen, because of its hot core alignment process and rotational fiber holders.

The process is the following. The fiber is rotated manually in order to minimize the eccentricity in the orthogonal viewing planes of the cameras, fig.3.4. Then the *RTC* sequence begins. The splicer applies a sequence of increasing currents to heat the fiber to the point where the core becomes visible and its offset can be measured.

This technique has been used for a large part of the present work since it gives significantly better results, tbl.3.3, than the method n°1.

min	max	avg	stdev	success
0.14	2.59	1.45	0.87	53.52%

Table 3.3: Splicing method n°2 - Insertion loss [dB]

The main improvement is the decrease of the standard deviation (around 59%), that makes this method far more reliable considering the quality of the splices.

Nevertheless, it didn't give entire satisfaction. The core was found in around 53% of the attempts. When not found, the current went so high that the fiber tip was damaged and needed to be cleaved again.

Moreover, that splicer requires a longer length of bare fiber, because of the fiber holder design that include an extra vacuum pump. The etched setup of *PaDo* and *PaDowH* needed to be 20 cm as more, complicating an already critical handling process.

Due to those problems leading to a poor yield, a third technique has been investigated.

3.5.4 Method n°3 - *FSU 925 RTC* with power measurement

The third and last technique used to splice the *PaDo* and the *PaDowH* is all manual with laser source and power meter, fig.3.6.

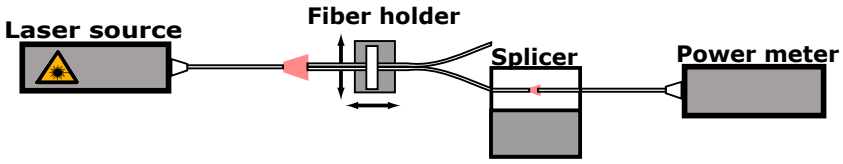

Figure 3.6: Splicing scheme with laser source and power meter.

A laser source is connected with a pigtail whose bare tip is cleaved to let the light spread out. This expanding beam is collected by one of the arms of the *PaDo*. The power meter allows to identify which arm is illuminated. This arm is then put in the splicer.

Through the use of the fiber holder, the positioning of the *PaDo* is tuned to maximize the transmission of light through the fibers. Depending on the open space between the laser source and the cleaved *PaDo*, the value of the loss is around $15dB$, that is still measurable with accuracy when using a $-4dBm$ light input.

Finally, the *PaDo* core is manually placed in front of the pigtail's core by measuring the transmitted power. And the manual splicing process of the splicer is issued.

This technique gives the best results so far. The bare length of *PaDo* needed to fit in the splicer is much less than in the 2^{nd} method, typically 12 cm. Thus, the handling of the setup is made easier.

Concerning the performance of this method, it gives satisfactory results since the insertion loss is significantly decreased. The lowest loss obtained was of 0.05dB, and the standard deviation is also the lowest obtained. Finally, because it does not use the *RTC* sequence the success rate is of 100%, tbl.3.4.

min	max	avg	stdev	success
0.05	1.5	0.53	0.56	100%

Table 3.4: Splicing method n°3 - Insertion loss [dB]

The following picture shows the splice of a *PaDo* with a *STF*, fig.3.7.

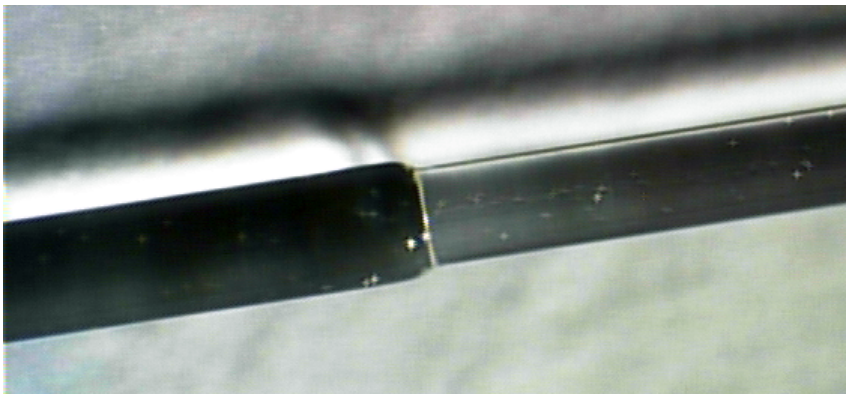

Figure 3.7: Splice between *STF* and *PaDo*

The radius difference between both fibers is really noticeable.

3.6 Conclusion

The *PaDo* and *PaDowH* are now connected at their 4 ports. The connections are finally taped two by two on an Aluminum plate, that allows to strengthen and also move the setup without problems, fig.3.8.

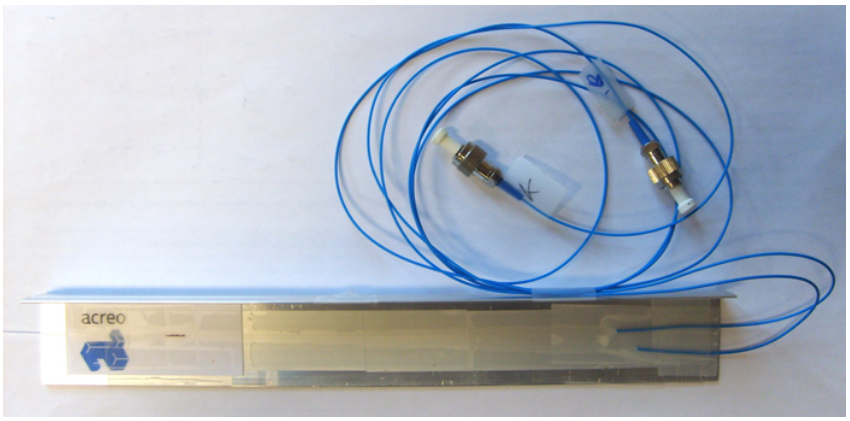

Figure 3.8: Finished setup of a spliced *PaDo*. The coated *PaDo* is on the left and the two spliced ports on the right. The previous stage with the cardboard, fig.3.3, is taped on the aluminum plate.

The handling process to build an exploitable setup made of *PaDo* or *PaDowH* is fully controlled. However, the time needed to go through those 6 steps is approximately 4 hours, if nothing is brocken.

Chapter 4

Characterization

Once the setup is made, it is possible to launch light into the fibers and see how they react. Two measurements used to characterize the fibers were the Polarization Dependant Loss and the Differential Group Delay[1][12].

4.1 Definitions

The *PDL* is expressed here as the ratio of the minimum to maximum transmission of the device in dB when all possible polarization states are scanned. In other words, $PDL = -10\log(T_{min}/T_{max})$.

This value tells us about the polarization dependance of the device. For example, a perfect polarizer has infinite *PDL*, and a perfect fiber has *PDL* zero.

In the case of *PaDo* and *PaDowH*, it can be considered as a measure of the roundness of the core and the effect of the stress due to the atypical geometry of the fibers. This geometry can induced an asymmetry in the core leading to a preferred polarization state of propagation, and thus to a high value of the *PDL*.

The *DGD* is the delay between the two orthogonal principal state of polarization. For a very long fiber length, it is a random process since it depends on the details of the birefringence along the entire fiber length. It is then also sensitive to temperature and mechanical perturbation in the fiber. For a short fiber length, the *DGD* is a well defined quantity.

This measure is then an insight of the birefringence of the core of *PaDo* and *PaDowH*. Similarly to *PDL*, some birefringence can be induced by the special double geometry or the presence of holes close to the core for *PaDowH*.

4.2 Scheme of the measurement

The setup is the same for both *PDL* and *DGD* measurements. A tunable laser source, TUNICS-Purity from *Photonetics*, is connected to a Polarization Measure-

[1] respectively abbreviated to *PDL* and *DGD*

ment System, PAT9000B from *Thorslab*. This machine includes a module to rotate the output polarization, a polarization analyzer and the software needed to exploit the measures.

The characterization was made on 4 meters long setup of *PaDo* and *PaDowH*. An etalon made of the same length of *STF* was also measured for comparison.

4.3 Measurement of *PDL*

The *PDL* is measured with regards to the wavelength for each fiber type, fig.4.2 - p.20.

Concerning the measured data, it is clear that the trend is conserved on each arms of the *PaDo* and *PaDowH*, and that the order of magnitude of the *PDL* is the same for all fibers and for both arms, tbl.4.1.

fiber	min	max	avg
STF	0.067	0.114	0.091
$PaDo1$	0.050	0.186	0.096
$PaDo2$	0.082	0.188	0.134
$PaDowH1$	0.043	0.166	0.088
$PaDowH2$	0.007	0.169	0.078

Table 4.1: PDL[dB] in *STF*, *PaDo*, and *PaDowH* for one measurement. Both arms in *PaDo* and *PaDowH* are measuremed independently.

However, the values exhibit dispersion. For example, there is a 28% difference between the average *PDL* value in dB between both halves of *PaDo*, namely $PaDo1$ ($0.096dB$) and $PaDo2$ ($0.134dB$).

To obtain a more precise insight of the *PDL* dispersion in those studies, several measurements were then made on the *PaDo* setup. Repeatability in time and between different arms is checked during this process, fig.4.1.

According to the curves, one might observe that the behavior is shifting significantly with regards to the wavelength, and that the level of noise is quite comparable to the expected value. The average and standard deviation for each value is thus computed, tbl.4.2.

The first two lines show the result for the two arms of the *PaDo*setup, while the third one shows the average results of all the measurements. On each line, the minimum, the maximum and the average value for the average and standard deviation of the *PDL* are presented.

The main result in this table may be the 20% difference between the average *PDL* value between the arms $PaDo1$ ($90.5 \cdot 10^{-3} dB$) and $PaDo2$ ($113.5 \cdot 10^{-3} dB$) of a *PaDo*.

Since the difference is decreasing when an average is made, one can suppose that it tends to be negligible. This occasional difference may have several causes :

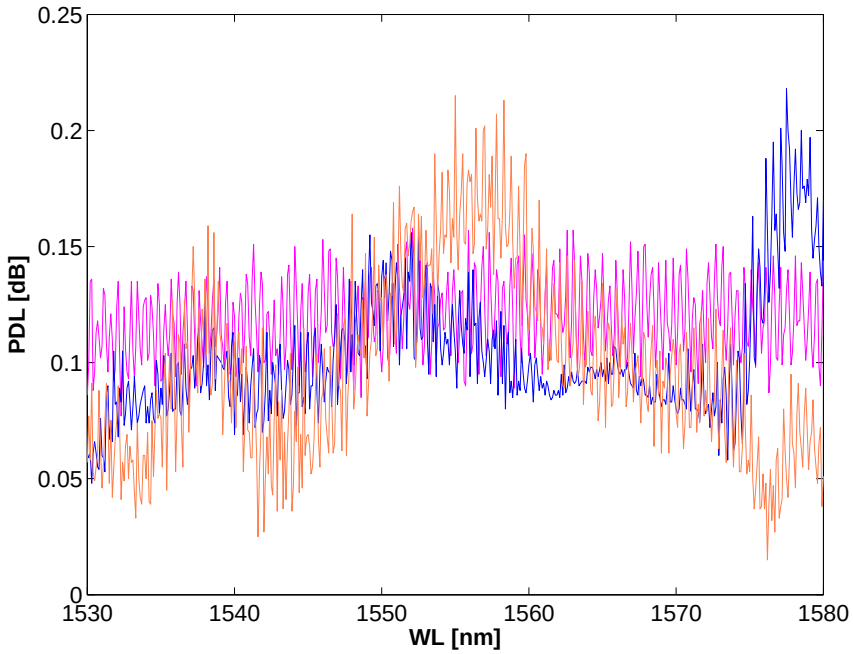

Figure 4.1: Consecutive *PDL* measurements for one *PaDo*setup. The measurements exhibit a high dispersion.

	avg			stdev		
fiber	min	max	avg	min	max	avg
*PaDo*1	48.0	136.5	*90.5*	41.0	30.4	40.3
*PaDo*2	48.8	230.8	*113.8*	35.9	34.7	26.0
PaDo	52.4	199.4	*108.9*	31.3	48.8	27.2

Table 4.2: Comparison of average$[10^{-3}dB]$ **and stdev**$[10^{-3}dB]$ **of *PDL* for *PaDo* setups**

mechanical stress on the fibers during the measurements, temperature fluctuations or more likely a difference in the quality of the splices.

Anyhow, for the value of the *PDL* remains in the same order of magnitude as with a *STF*, the conclusion drawn is that the *PDL* in *PaDo* and *PaDowH* is comparable to the standard ideal value. This allows to use these fibers without a special interest in the input polarization.

4.4 Measurement of *DGD*

The same process is applied for the *DGD* measurement. When the length of the device is short as compare to the coupling length l_c, the expected distribution of the measured *DGD* is a delta function, whereas for a long-length regime, the distribution

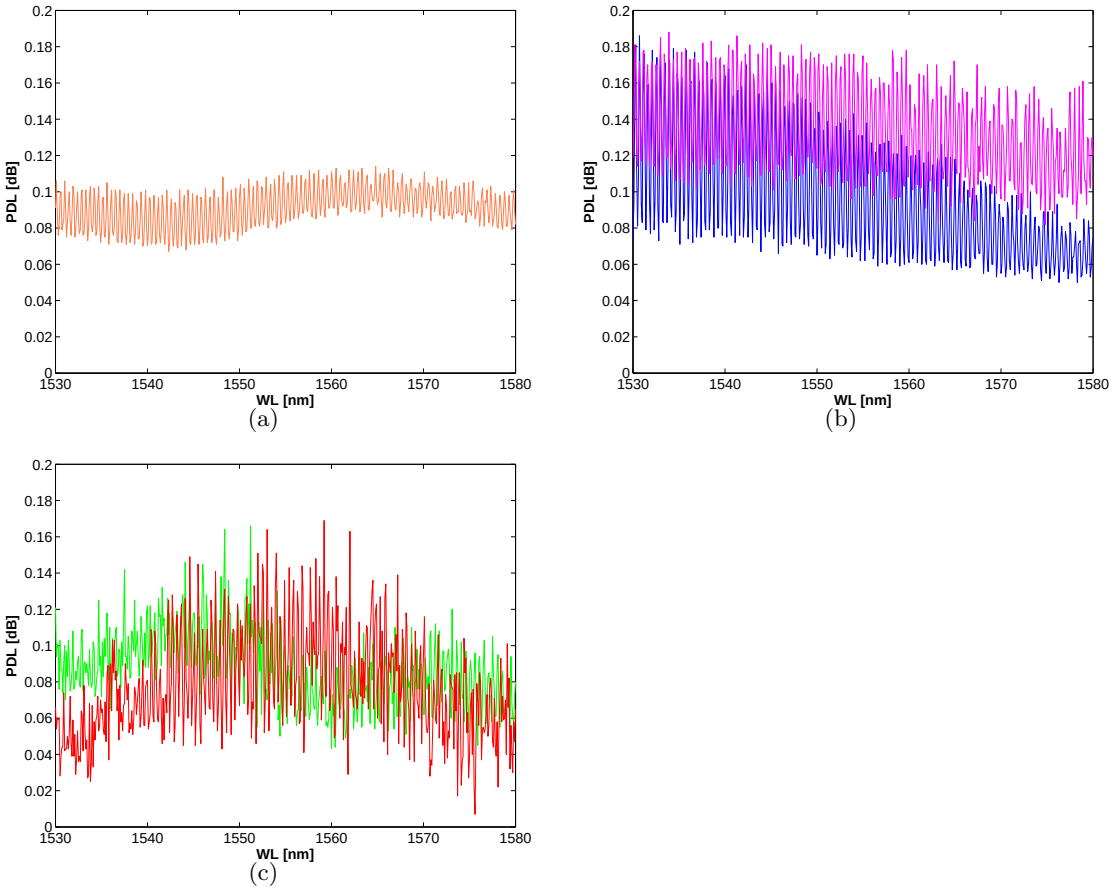

Figure 4.2: *PDL* measurements in *STF* (a), in both *PaDo*'s arms (b), in both *PaDowH*'s arms (c).

is maxwellian.

In a typical *STF*, the coupling length is of the order of 10 meters. This means the three setups are expected to be in the short-length regime if *PaDo* and *PaDowH* do not exhibit a high birefringence, since the samples are 4 meters long.

One measure for all setups is presented in fig.4.3. As expected, the distribution for the *STF* is very sharp, even if the presence of noise broaden the peek. Concerning the *PaDo* and *PaDowH*, the distribution is less sharp, but still exhibits a main value in the same order of magnitude.

Several measurements are made. The next table, tbl.4.3, shows the results for 1 measures on the *STF* setup, an average of 4 measures for the *PaDo* setup, and an average of 2 measures for the *PaDowH* setup.

The *DGD* value is $66,7\%$, respectively $75,6\%$, higher than the ideal value of the *STF* for the *PaDo*, respectively *PaDowH*. It still remains in the same order of magnitude and is acceptable for an optical component.

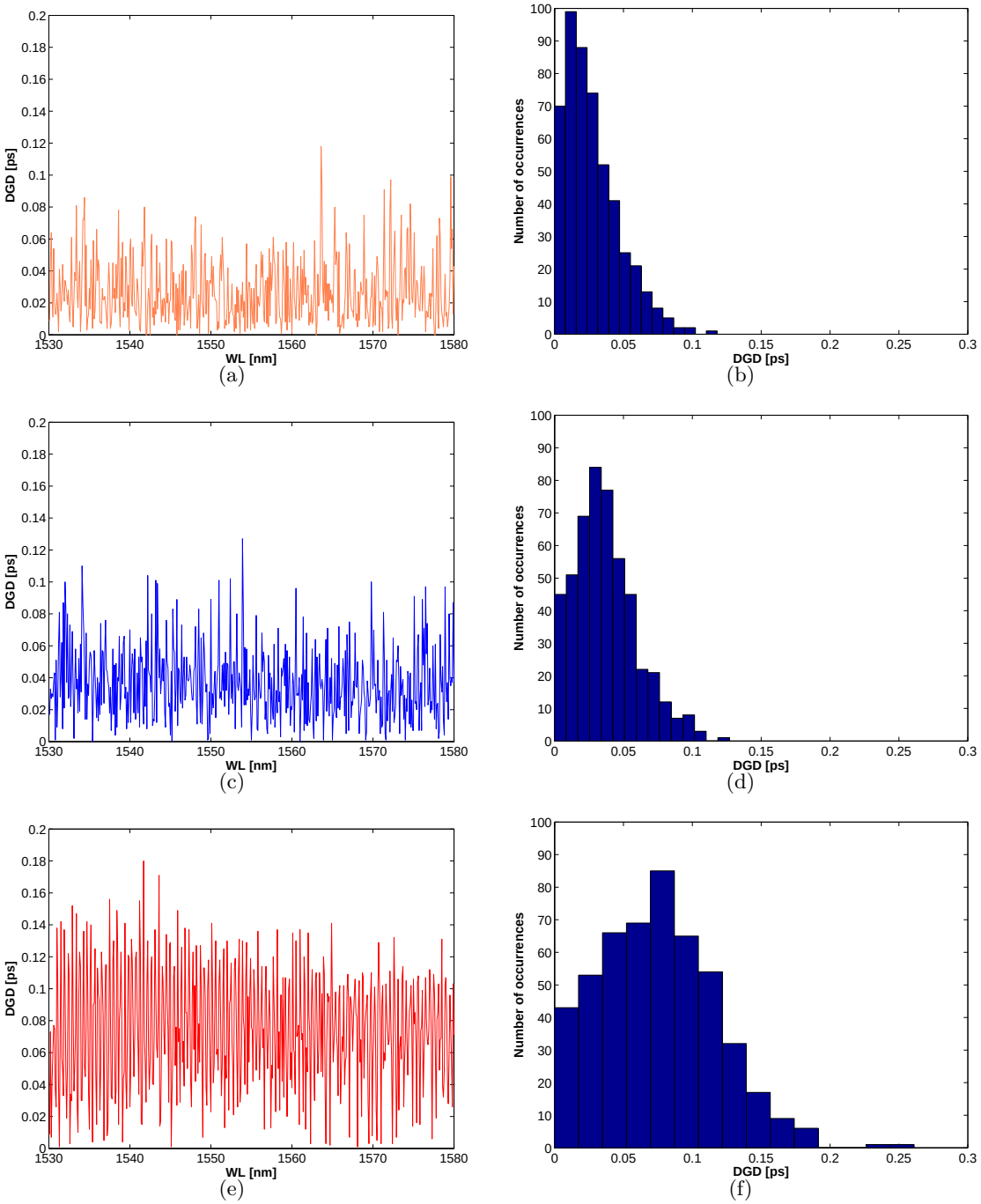

Figure 4.3: ***DGD*** **versus wavelength and histogram for** ***STF*****(a,b),** ***PaDo*** **(c,d), and** ***PaDowH*** **(e,f).**

fiber	avg	stdev
STF	27	–
PaDo	45	6,3
PaDowH	74,4	0,7

Table 4.3: DGD in average$[10^3 ps]$ **and stdev**$[10^3 ps]$ **for *STF*, *PaDo*, and *PaDowH*.**

In addition, when *PaDo* and *PaDowH* will be used, the effective length will be shorter than 4 meters, typically $0.5m - 1m$. The *DGD*, that scales as linearly with the length of the device in the short-length regime, will be reduced by a non negligible factor.

Furthermore, the assumption on the length regime can be checked by analyzing the measurement data as stated in [12].

Two quantities are introduced : N_e, the total number of maxima and minima in a defined frequency window, and N_m, the total number of mean-value crossing of the transmission in the same defined window.

The following relations hold true :

$$\frac{< N_e >}{< N_m >} = 1,54 \qquad \text{when } L/l_c \to \infty$$
$$\frac{< N_e >}{< N_m >} = 1 \qquad \text{when } L/l_c \to 0$$

where L is the length of the device, and l_c the characteristic coupling length. This ratio is computed [2] with Matlab and averaged over the measurements, tbl.4.4.

fiber	avg	% of 1.54
STF	1,4537	94,4
PaDo	1,3065	84,8
PaDowH	1,3259	86,1

Table 4.4: Regime ratio and its percentage of long length ratio in *STF*, *PaDo*, and *PaDowH*.

However, this method is accurate only if the statistical uncertainty of the measurement procedure is significantly better than 50%. Considering the rather small value of the *DGD*, and the noise exhibited on the previous curves, fig.4.3, it is clear that the precision of the measure is not high enough to obtain valid results.

That explains why the 4 meters long fibers of all types are supposed to be in the long-length regime, tbl.4.4, according to their value of the ratio close to the long-length regime value.

[2] by the use of the functions *extrema* from *Carlos Adrián Vargas Aguilera* and *crossings* from *Christos Saragiotis*, see source code in D.4 - p.78

4.5 Conclusion

The measured value of *PDL* and *DGD* as compared to an equivalent setup of *STF* validates the quality of the manufacturing process. So to say, the quality of the fiber is not altered by the fact that they are drawn and glued by pair.

Finally, the *PaDo* and *PaDowH* will be used without additional control of the input polarization, just as a *STF* will be.

Chapter 5

Making a directional coupler - part.1

The first step toward an interferometer is to do a coupler in the fibers, for it is the equivalent of a beam splitter. The phenomenon responsible for the coupling effect between two fibers is the wave coupling that occurs when the waveguides are brought close enough one to another. According to the literacy[1], two main methods have been investigated to produce the coupling.

One is to polish the fibers to the core before gluing them along the polish section. The other one is to make a taper by melting and pulling two adjacent fibers[14, 15]. The latest, now the standard in the industry, is more suitable with regards to the *PaDo* and *PaDowH* geometry. The melting and pulling technique is thus used in the thesis.

This chapter presents first a quick description of the phenomena involved in the coupling effect, some considerations about the taper geometry, followed by the explanations on the process and the results obtained on a *STF*.

5.1 Main effects and mathematical description

A coupler can be described as a double taper made of two fiber. The fibers are heated, first melted together and then pulled. The coupling effect is the resultant of two associated phenomena :

- the mutual excitation of two adjacent waveguides

- the expansion of the field in the cladding

Concerning the coupling, the famous coupled mode equations formalism[16] can be used to explain the mutual coupling that appears between closely spaced waveguides. More precisely, it shows that the transert of power occurs since the field

[1]Extensive work on the coupler component in fiber has been achieved by the groups of S. Lacroix and J.D Love. Besides, they published a paper together about the adiabacity criteria in tapered single-mode fiber [13].

distribution in one fiber is broad enough to start exciting a mode in the second waveguide. As a result, the light starts being guided in this second waveguide.

Concerning the expansion of the field, the decrease in fiber-core radius in a taper leads to a corresponding increase of the local-mode spot size, which for a sufficiently small fiber-core radius causes the mode field to extend to the fiber cladding-external medium interface[17].

In other words, as the radius of the fiber decreases, the core goes down in diameter and the field tend to spread out in the cladding until the point when the core-cladding medium is completely filled with the light wave.

S. Lacroix's group showed that the combination of the two phenomenon is compulsory to obtain the strong coupling[14] in such a structure. So to say, to couple the light between two fibers is not feasible by the only means of evanescent waves.

Indeed, the value of the coupling factor, see α in (5.2), is computed through the overlap integral, the overlap between one field and its adjacent waveguide. The expansion of the field in the cladding leads then to the high value of the coupling coefficient.

This decrease in diameter is mandatory to obtain the coupling, but can be responsible of undesirable side effects in the coupler that will be explained in the following section.

As an example, the transfer matrix of a lossless 2 x 2 fused-fiber coupler of length L is given by [18]:

$$T_{2*2}(\alpha) = \exp(\boldsymbol{i}\overline{\alpha}) \begin{bmatrix} \cos(\alpha) & \boldsymbol{i}\sin(\alpha) \\ \boldsymbol{i}\sin(\alpha) & \cos(\alpha) \end{bmatrix} \tag{5.1}$$

with

$$\alpha = \int_0^L \frac{B_{01}(z) - B_{11}(z)}{2} dz \qquad \overline{\alpha} = \int_0^L \frac{B_{01}(z) + B_{11}(z)}{2} dz \tag{5.2}$$

where $B_{01}(z)$ and $B_{11}(z)$ are the LP_{01} and LP_{11} local supermode propagation constants, respectively.

For the case of a coupler with an input in one arm, the output power in transmission in the cross arm is the following :

$$T_{cross} = (\begin{bmatrix} 1 & 0 \end{bmatrix} * T_{2*2}(\alpha) * \begin{bmatrix} 1 \\ 0 \end{bmatrix})^2$$

so to say :

$$T_{cross} = (1 + \cos 2\alpha)/2 \tag{5.3}$$

The behavior of the power is thus expected to be the following[2], fig.5.1. It starts coupling from the beginning of the coupler, and exhibits a complete oscillation of the power from one core to the other with a period of π/κ.

[2] with $\kappa l = \alpha$, and l the length in the coupler

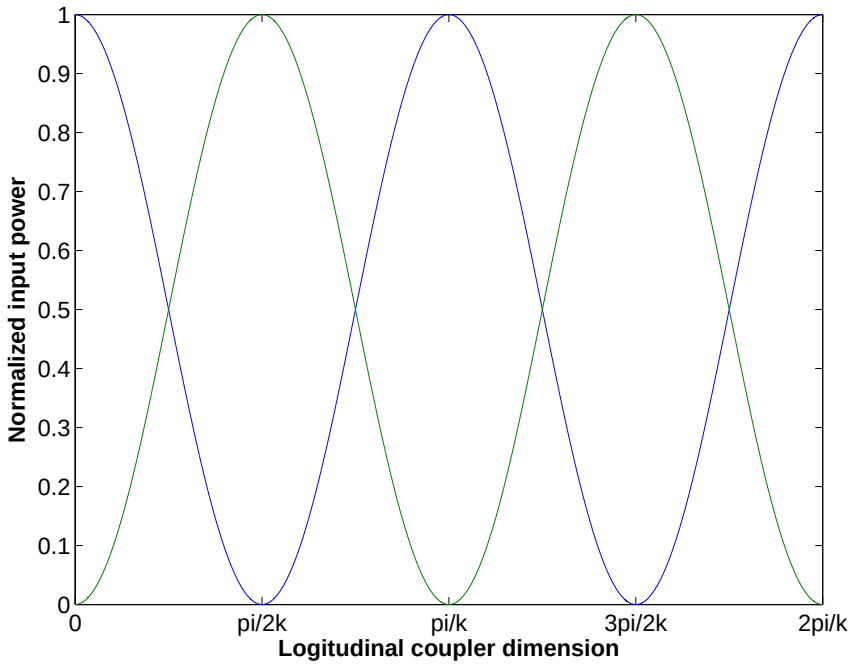

Figure 5.1: Theoretical oscillation of the power in a coupler. Each color represent one arm in the coupler.

The points where the curves are crossing are the points where the power equally split among the arms, such a coupler is called $-3dB$ coupler.

5.2 Taper geometry

As stated above, to obtain the coupling effect, a taper structure has to be made in the coupling region, where the fibers are brought close to each other.

The geometry of a taper, made with the melting and pulling, has been the subject of an article [19], which proposes a model according to some fluid dynamics considerations. The fig.5.2 explicits the conventions.

Several variables are defined. The hot zone L_0 is the length that is heated during the process. The final taper shape is uniform and cylindrical. It is defined during the process by its length l_w and its radius r_w. The taper extension x is the net extension applied to the fiber, while z is the longitudinal coordinate used to measure the length in the taper. The origin is set at the beginning of the unstretched fiber, which radius is r_0. Finally, r is the varying radius in the taper transitions.

According to the literacy, when the hot zone is constant, the followings relations hold true :

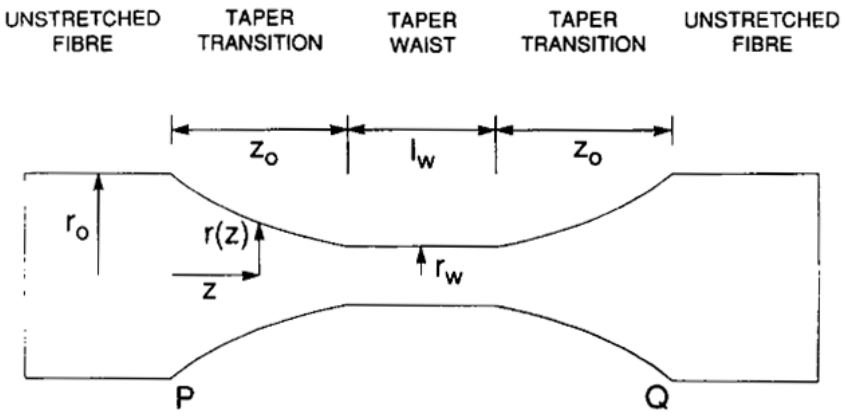

Figure 5.2: Model of a taper drawn with the melting and pulling method, according to [19].

$$z(x) = x/2 \tag{5.4}$$
$$r(z) = r_0 e^{-z/L_0}$$

thus,

$$\frac{dr}{dz} = -\frac{r_0}{L_0} \cdot e^{-z/L_0} \tag{5.5}$$

The profile of the taper transition is approximated by an exponential while the heated tapered zone width l_w is supposed to be constant, with a flat profile. By setting the value of the hot zone length L_0 and the net extension x, it is then possible to predict the slope of the transition and the final width.

Those characteristics are of great importance when it comes to deal with the taper performances since two main effects appears in this kind of structure.

As explained above, as the radius of the taper decreases, the light starts being guided by the whole fiber. The normalized frequency is a good indicator to quantify this phenomenon. It is defined as :

$$V = \frac{2\pi}{\lambda} a n_1 \sqrt{2\Delta} \tag{5.6}$$

where n_1 and n_2 is the index of the core, Δ the difference between the index of the core and the index of the radius, and a the core radius.

The local-mode spot size increases when the normalized frequency decreases, and when V is approximately equal to unity[14], in the case of a single mode fiber, the mode field can be considered to extend to the cladding-external interface.

Second, the slope of the taper define how well the fundamental mode will couple into the taper structure. If the taper transitions are too abrupt, the fundamental mode will be partially decomposed over higher modes, propagating through the structure with different propagation constants. At the end of the structure, depending on the relative phase-shift, the modes will create interferences that induces a modulation in the transmission. A condition over the slopes defined if the structure is adiabatic or not[13]:

$$|\frac{dr(z)}{dz}| \leq \frac{r(\beta_1 - \beta_2)}{2\pi} \tag{5.7}$$

where β_1 and β_2 are respectively the local propagation constants, in the transition, of the fundamental mode and the mode to which the power is most likely to be lost.

Those two effects are very important when a coupler is being made, since they affect its performances.

5.3 Definition of the process

The machine used to make a coupler is a large diameter splicer (LDS-1250) from Vytran Corporation. It is composed of two lateral fiber holders driven by independent step motors and a motorized central heating system, based on a resistive Iridium filament with an Argon flow controller, fig.5.3.

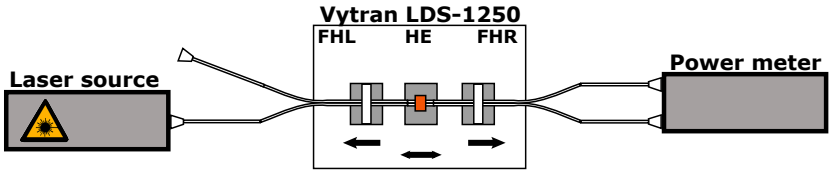

Figure 5.3: Coupler making scheme

The machine is also connected to a computer through a COM port cable, that allows to program the memory and load it with the macro written by the user.

The coding language is rather simple. A macro is composed by a list of command which syntax is defined as following, in fig.5.4.

command([device_id] parameter_value)execution_time ;comments

Figure 5.4: Command syntax for the LDS1250

Each command can influence an optional machine device through the use of its ID, see B.2-p.69, and takes one parameter value.

There is mainly three families of command used to build a macro.

a. the motors control commands

The motors of both fiber holders and heating system are controlled in speed. The unit is $[steps/sec]$ and one step is equal to $0.8\mu m$. The motion is limited in range, and the motor can toggle if the limit is reached, otherwise it will stop. Here is a set of typical instructions :

```
motordatum(8 0)                    ;M8 cur_pos = 0
motorvel(8 25)20                   ;M8 speed 25
motorlimits(9 -3500 3500)40        ;FMT range to +/-3500
motorexstep(7 -3500)50             ;M7 motion to -3500
setmotortoggle(9 1)                ;M9 toggling on
```

b. the filament and Argon control commands

The filament temperature and the Argon flow are controlled through the numerical value of their respective DAC. A calibration curve gives the equivalent in temperature for the filament, **??**-p.**??**, while the Argon flow calibration is given in the Vytran documentation.

```
enablefilament(1)10                ;FMT enabled
setdac(5 50)20                     ;FMT current to 50
setdac(4 2500)20                   ;ARG flow to 1l/min
```

c. the execution time control

The execution time of each command is controlled in two ways. A time counter is started at the beginning of the macro. The tag following each command defined its execution according to the counter. A special command, *macropause*, first resets the counter and second wait a defined time (in $msec$) or a defined event to continue the execution of the macro, for example :

```
macropause(0x1D 130000)            ;wait M7 or Xmsec
```

allows to wait for the left motor to finish its motion, or 130 secondes.

Regarding the possibilities offered by this language, a sequential process is elaborated. It is composed by the same distinctive blocks that are tuned to improve the process :

1. Filament/Argon flow init procedure
2. Filament enablement and temperature increase
3. Motor motion n°1
4. Motor motion n°X

The process includes several motor motions, distinguished by their differences in speed/range of motion. Each process can then be presented as following :

	T[°C]	$V_{7,8}[\mu m/s]$	$L_{7,8}[\mu m]$	$V_9[\mu m/s]$	$L_0[\mu m]$	$t[s]$
motion 1	1800	100	3000	1500	4000	100
...	...	...	...	...	...	...
motion x	1900	100	3000	1500	4000	100

Table 5.1: Vytran parameters for program X

where the subscripts represent the ID of the device, namely 7 and 8 are the left and right motorized fiber holders, and 9 is the filament motor.

Because of the conception of the device, the macro once launched is not supposed to be tuned, as opposed to the process showed in [7, 9]. Such as no integrated feedback loop system or integrated measurement made on the fiber through the process is computer controlled. Thus, the only method used to monitored the process is to launch light into the fiber and measure the transmitted intensity as a function of time.

5.4 Elaboration of the process with STF

At Acreo, some previous work had already been done with this machine, but no protocol had been defined to realize a taper or a coupler. The first tests are then made with a *STF* to train on the process. This section presents the investigations steps to obtain an adiabatic taper.

5.4.1 First results

The setup is the same as presented in fig.5.3 with the only difference that a *STF* is placed in the Vytran. Then, a macro is launched and the transmission is monitored as a function of time.

The first results exhibit a very high deviation in the behavior of the transmission, fig.5.5, that hinders from having a repeatable process. The measurements obtained are erratic with the same experiments parameters.

The process of heating and drawing a fiber leads to such perturbations in the fiber structure that it has to be gentle. Several factors are taken into account : the speed of the three motors, the elongation value, the length of the hot zone, the temperature of the filament, and the power of the argon flow.

Those parameters are set to their lowest acceptable value[3], so that a repetitive process is obtained and the influence of each can be determined.

After several attempts, the parameters in tbl.5.2 are set to constitute the default parameters used in the development process. The transmission with regards to the elongation time is plotted in fig.5.6 , and has been shown repetitive.

[3]Provided that a taper is still made - or that the fiber is soft enough to be drawn.

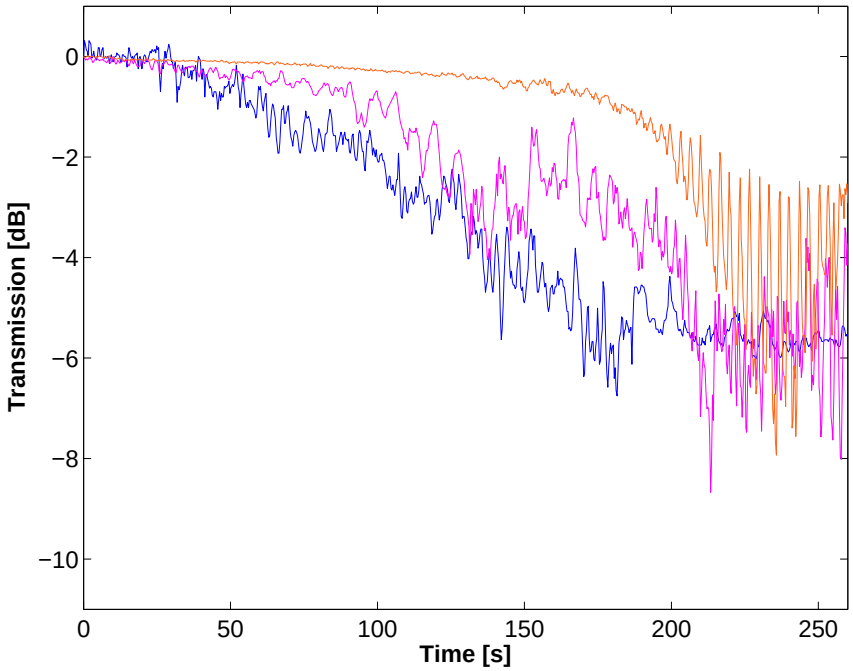

Figure 5.5: Effect of tapering on *STF*

The beginning of the process, (0-100sec), induces perturbations in the fiber transmission in the order of $0.2dB$. Which is very little as compared to the following phase (100-300sec) where the transmission drops to $-4dB$ and starts oscillating with a maximum amplitude of $6dB$. Futhermore, the value of the peaks seem to follow a decreasing trend.

Among other, three different symptoms are identified :

- increasing loss due to metal deposition and oxidation
- high amplitude oscillations related to a non-adiabatic process
- transmission fluctuations due to temperature perturbations

5.4.2 Improvements

Since the previous macro leads to a repeatable behavior, it is now possible to improve the process with the help of the model and by tuning one by one the parameters.

a. Validity of the model

The first step is to check the validity of the model. To do that, a special taper is drawn with the following parameters, tbl.5.2. The hot zone length is the same as with the reference taper but the elongation is longer.

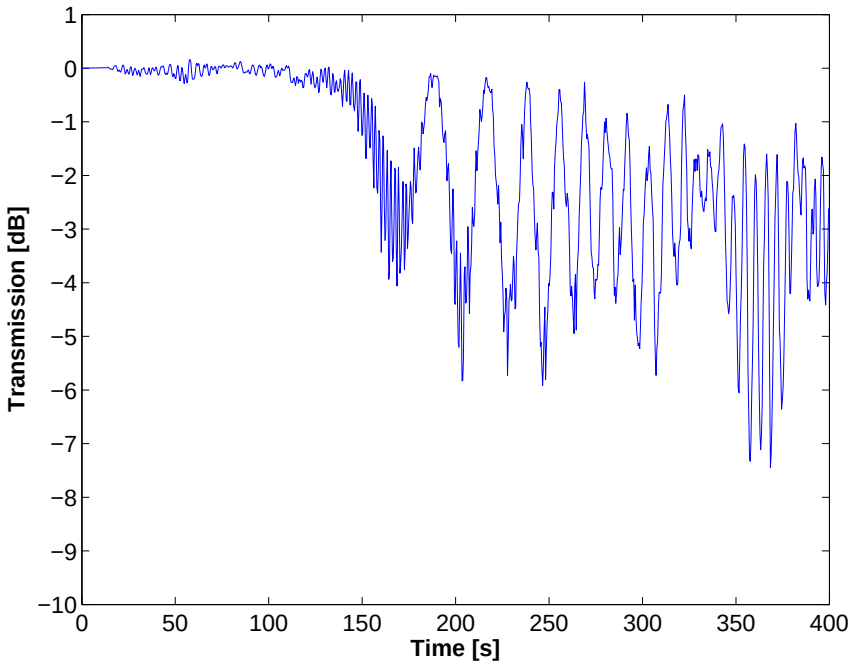

Figure 5.6: Measured transmission through a *STF* when tapering with the reference program.

	T[℃]	$V_{7,8}[\mu m/s]$	$L_{7,8}[\mu m]$	$V_9[\mu m/S]$	$L_9[\mu m]$	$t[s]$
motion 1	1543	16	x	1600	±1600	x

Table 5.2: Vytran parameters for the reference taper

	T[℃]	$V_{7,8}[\mu m/s]$	$L_{7,8}[\mu m]$	$V_9[\mu m/S]$	$L_9[\mu m]$	t[s]
motion 1	1543	24	x	1600	±1600	165

Table 5.3: Vytran parameters for the special taper

Under an optical microscope, the taper width in the transition is measured. The comparison between the supposed taper shape and the computed one is drawn, fig.5.7. The blue curve is plotted from the raw data, while the magenta one is smoothed.

From the figure, the model shows itself to be interesting but not very accurate. The hypothesis more likely not to be fulfilled is the temperature distribution. It is unrealistic to consider it to be a boxcar function centered over L_0, implying that directly outside, the temperature is ambient. This is the reason of the smoother transition when z is smaller than $1000\mu m$.

Considering the final width of the taper, the values given by the model (r_{th}) and the experiments (r_{ms}) can be confronted. According to tbl.5.3, one will obtain for

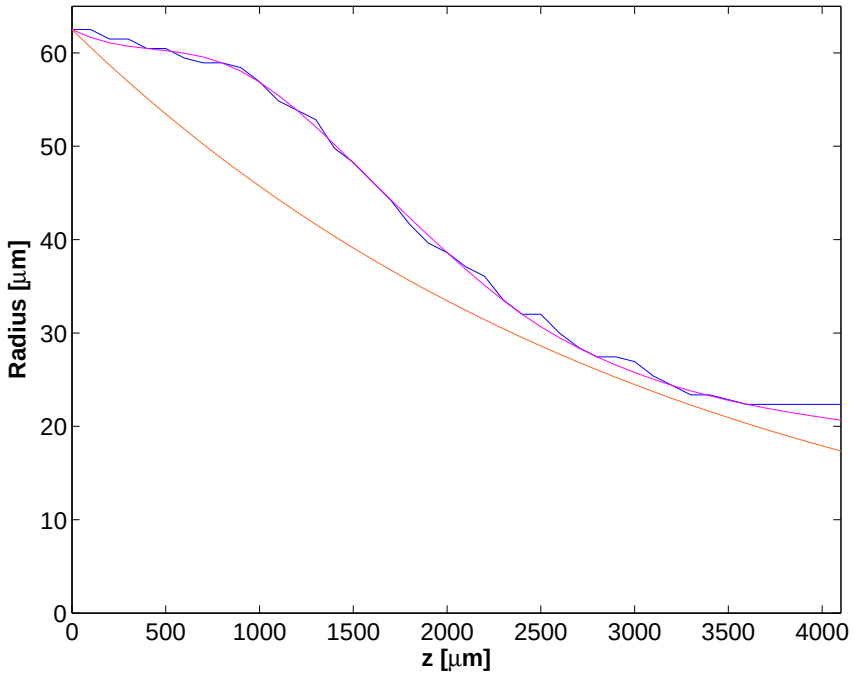

Figure 5.7: Comparison between the reference taper recorded profil in blue and magenta and the model in orange.

the elongation :

$$z = 24.10^{-6} \cdot 165 = 3960\mu m$$

that leads with the equation (5.5) from the modeling to :

$$r_{th} = 125.10^{-6} \cdot e^{-3960/3200} = 18.1\mu m$$

while the measured value for the same z gives :

$$r_{ms} \approx 21\mu m$$

The real final value of the taper width is 13% bigger than the theoretical value, which is considered to be acceptable.

An other interesting characteristic is the derivative of the taper transition, which is related to the adiabatic criteria, as shown in (5.7).

The derivative of those two functions are plotted in fig.5.8. Here however, it is clear that the real derivative isn't well described by the model. The maximal value, comparable for the two curves, does not appear at the same place in the taper. And for most of the curve, the real value is at least twice as great.

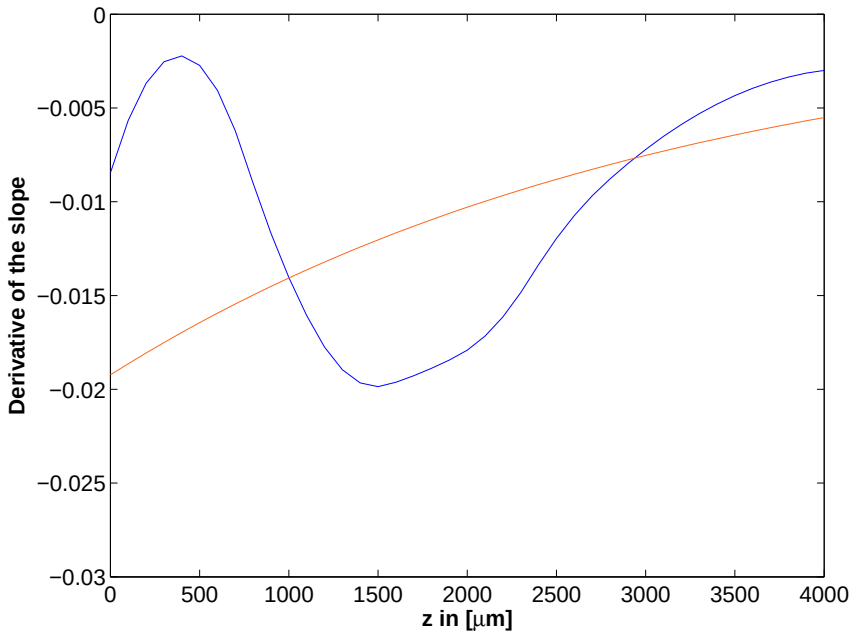

Figure 5.8: Comparison between the slopes of the reference taper (in blue) and the model (in orange)

The adiabatic character of the structure can be questioned. The value for the inequality are then to be calculated. From [20] - p.35, the value for β_1 and β_2 can be obtained :

$$\beta_1 - \beta_2 \approx \frac{\Delta n \cdot 2\pi}{\lambda}$$

so to say,

$$\frac{r(\beta_1 - \beta_2)}{2\pi} \approx \frac{\Delta n \cdot r}{\lambda} \tag{5.8}$$

This function is plotted on fig.5.9 to compare the curves between the derivative and the adiabatic limit. Here the structure is supposed to be adiabatic since the inequality is satisfied over the whole structure. However, this special taper is found later to be non-adiabatic.

Several assumptions can be questioned. First, the approximation (5.8) might not be accurate enough. Second, the data plotted has been smoothed to produce a continuous curve, but the real process is quite traumatic for the fiber, and may produce such irregularities in the slopes, inducing peeks in the derivative.

Eventually, the model can be useful when it deals with predicting the final shape of the taper, but is shown unable to affirm with certainty wether the taper produced is adiabatic or not. Thus, a significant security margin is needed.

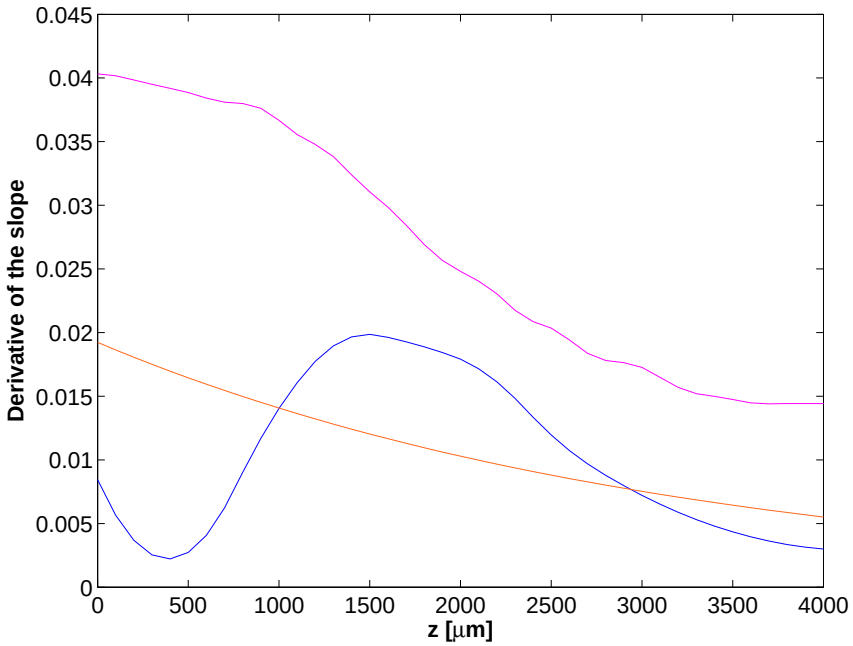

Figure 5.9: Adiabatic criteria, comparison between the members of the inequality (5.7)**. In orange/blue the left-hand side for the theoretic/measured slopes, in magenta the right-hand side.**

b. Influence of the parameters

In the meantime, the influence of the drawing speed, of the hot zone length and of the temperature has been investigated.

According to the theory, the drawing speed should not influence the process, as shown for three value of the speed, fig.5.10.

The behavior is clearly similar, meaning that the oscillations appears at the same elongation. Roughly, a relation inversely proportional exists between the time when the coupling starts and the speed of the elongation, tbl.5.4, that validates the model for the taper process.

The estimated value of the diameter of the taper when the oscillations appears, so to say approximately $60\mu m$ is really important. It gives a very good insight of the phenomenon in the fiber. As said above, the extension of the field in the structure is not supposed to occur before the value of the normalized frequency is equal to unity.

The value of the diameter at that particular frequency is computed. The fiber is a Corning STF-28, with the following parameters : $n_1 = 1.456$ and $\Delta = \Delta n/n$, with $\Delta n = 1.10^{-3}$. The wavelength of study is $\lambda = 1530nm$. With (5.6), one will obtain :

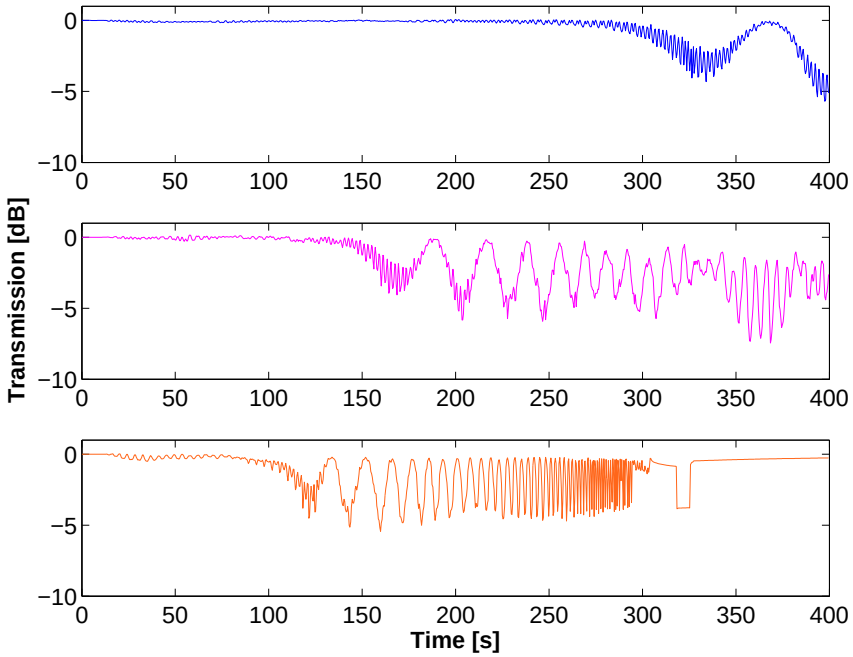

Figure 5.10: Influence of the drawing speed on the reference taper transmission. In blue $V_{78} = 8\mu m/s$, in magenta $V_{78} = 16\mu m/s$, in orange $V_{78} = 24\mu m/s$.

color	$V_{7,8}[\mu m/s]$	$t[s]$	$z[\mu m]$	$L_0[\mu m]$	$d_w[\mu m]$
blue	8	300	2400	3200	≈ 59
magenta	16	150	2400	3200	≈ 59
orange	24	100	2400	3200	≈ 59

Table 5.4: Relation of proportionality between coupling time and elongation speed.

$$d = \frac{\lambda V}{2\pi n_1 \sqrt{2\Delta}} d \qquad \approx 45\mu m$$

This value is 25% inferior to the modeled value of $60\mu m$. This means that the oscillations do not come from the perturbations of the field at the cladding/air interface, but from the perturbations induced by the change in the taper slopes.

One might conclude that the taper is non-adiabatic, and that the field is spread over higher mode producing these interferences in the structure.

The influence of the hot zone length is thus investigated, fig.5.11. As stated in the equation, by increasing the value, one might reduce the sloppiness of the transition and thus lead to less coupling in the structure.

Comparing the three curves shows the shape of the taper is affected by the hot

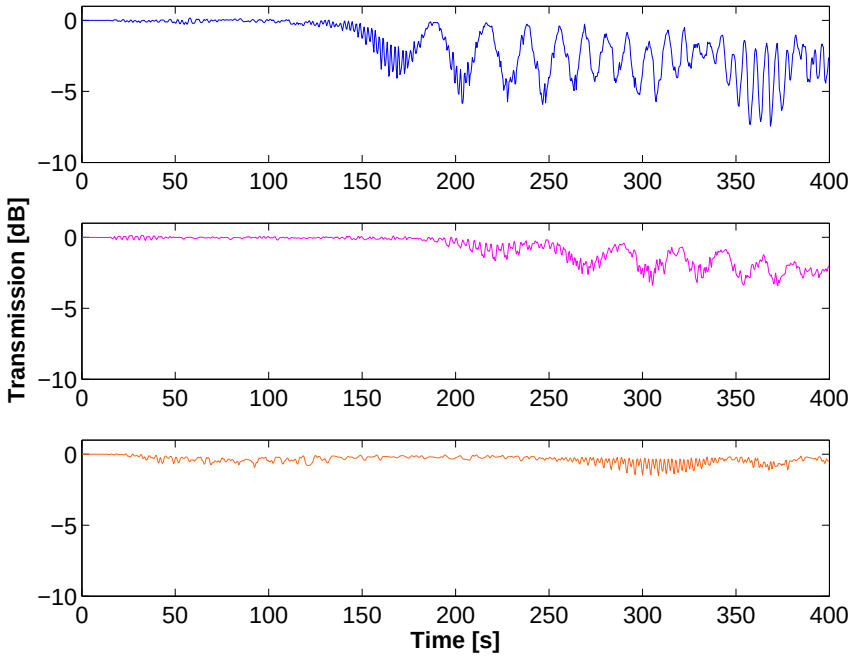

Figure 5.11: Influence of the hot zone length on the reference taper transmission. In blue $L_0 = 3.2mm$, in magenta $L_0 = 4.8mm$, in orange $L_0 = 6.4mm$.

zone length in a extensive way. The losses are reduced when the hot zone length is increased, and may eventually disappear, leading to an adiabatic structure.

However, with regards to the radius value at which the oscillations appears, tbl.5.5, it is not possible to predict when the structure will become non-adiabatic..

color	$V_{7,8}[\mu m/s]$	$t[s]$	$z[\mu m]$	$L_0[\mu m]$	$r_w[\mu m]$
blue	16	150	2400	3200	≈ 59
magenta	16	210	3360	4800	≈ 62
orange	16	280	4480	6400	≈ 62

Table 5.5: Influence of the hot zone length on the tapering process.

The main point to be concluded here is that the shape of the taper is affected by the hot zone length in a extensive way. It is not possible to say at which point the structure will become non-adiabatic.

Finally, the influence of the temperature, fig.B.1 - p.70, has been investigated, fig.5.12.

The fiber used is made of pure silica, and is thus supposed to melt at 1700°C, but of course a lower temperature is enough to soften the fiber to a point it can be stretched. The range of temperature used in this experiment shows that 100°Cis enough to jeopardize the process completely. When the temperature is too high

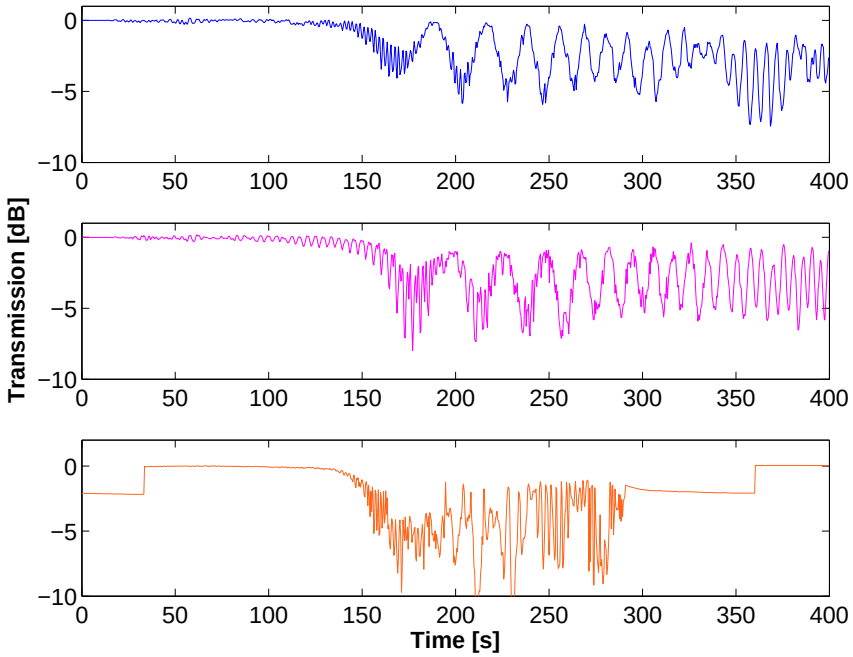

Figure 5.12: Influence of the temperature on the reference taper transmission. In blue $T = 1543$℃, in magenta $T = 1644$℃, in orange $T = 1689$℃.

the fiber is so soft that the local heated region shears transversely because of the softening, but also because of the argon flow and air currents, causing extra optical loss. This loss is characterized by a period equal to the period of the filament motion.

For example, the case of the reference taper program with a filament temperature of 1543℃ is taken, fig.5.13. The speed of the fibers holders is $16\mu m/s$ for a hot zone length L_0 equal to $3200\mu m$. That gives a period of $4s$ for a round trip over the hot zone. This value is consistent with the curve that exhibits five oscillations from $t = 140s$ to $t = 160s$.

5.4.3 Definitive process

In addition to all those informations, Suzanne Lacroix gave the few advices missing to realize a good taper. The rule of thumbs are : a $1cm$ hot zone length, a slow drawing speed and ten times higher for the scanning speed, leading to the final macro, tbl.5.6.

No figure of this is shown, the transmission is completely stable even after an elongation of 5 minutes, and a width going under the critic point where V is equal to one.

Remembering that a coupler is in some way a taper, the work on producing a

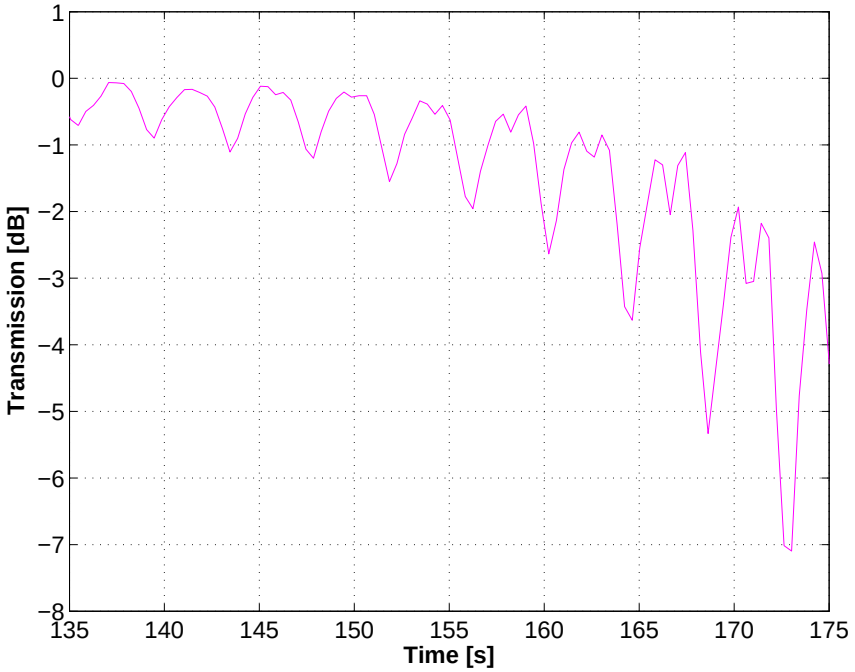

Figure 5.13: Shear loss on the reference taper program with $T = 1644$℃

	T[℃]	$V_{7,8}[\mu m/s]$	$L_{7,9}[\mu m]$	$V_9[\mu m/s]$	$L_9[\mu m]$	$t[s]$
motion 1	1543	24	x	240	$\pm$4800	x

Table 5.6: Vytran parameters for the final taper program, e.g. adiabatic.

coupler in *PaDo* can be launched.

Chapter 6

Making a directional coupler - part.2

Due to the geometry of the fiber, a small coupling already exist between the twin fibers, fig.6.1, and proves the *PaDo* a good predisposition to make a coupler.

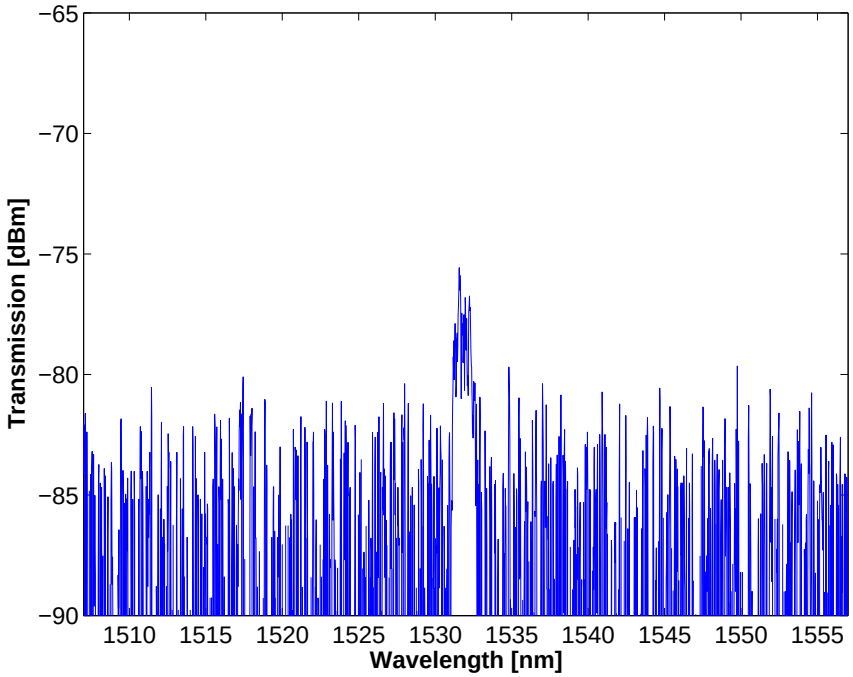

Figure 6.1: Auto coupling between both arms of *PaDo* with a $-20dBm$ input signal at $1532nm$. The recorded auto-couling is in the order of $-55dBm$.

6.1 First results with a non-adiabatic process - *Coupler A*

The process of making a coupler has actually been developed in parallel with the process of making a taper. So that the first result shows a coupler, called *Coupler A*,

done with the program close to the reference macro, tbl.5.2, and thus non-adiabatic.

	T[°C]	$V_{7,8}[\mu m/s]$	$L_{7,8}[\mu m]$	$V_9[\mu m/S]$	$L_9[\mu m]$	$t[s]$
motion 1	1613	20	2800	320	$\pm$2800	140
motion 2	1514	16	2400	160	$\pm$1600	150
motion 3	1514	9.6	1920	160	$\pm$1200	200

Table 6.1: Vytran parameters for the *Coupler A*

During the process, the evolution of the transmission in both arms is recorded, fig.6.2.

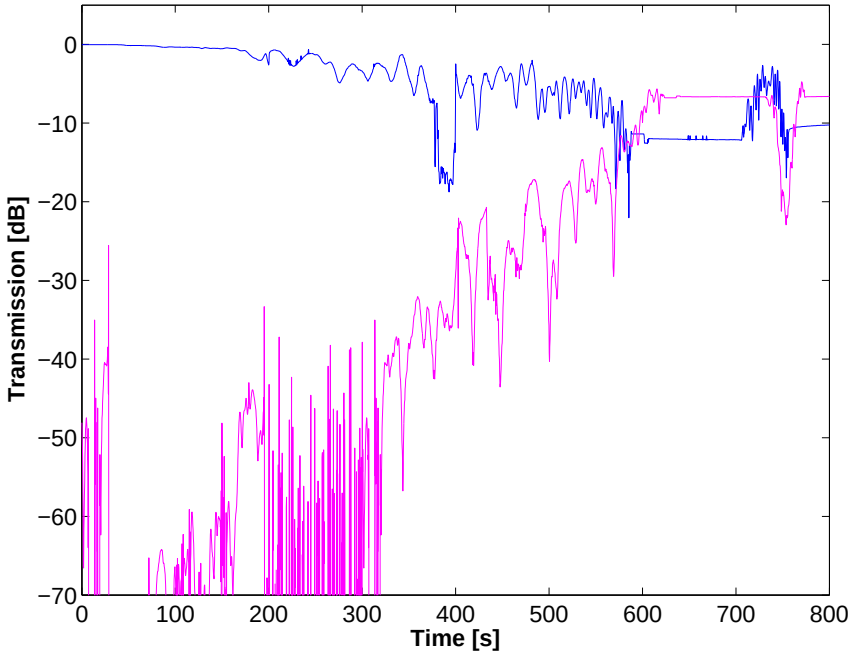

Figure 6.2: Coupling of light in *Coupler A*, cross arm (in blue) and straight arm (in magenta).

The light in the cross arm exhibits a $-70dB$ attenuation at the beginning of the process. The transmission is increasing approximately constantly to equal the one in the blue arm after 10 minutes. Finally, a slower elongation speed is applied in a try to equal the transmitted power in both arms and obtain a $-3dB$ coupler. However, the presence of oscillations leads to a very inaccurate tuning ; as shown at time $t = 700s$ when a small change in length can induce a temporary $10dB$ loss.

The opposite of the cumulative losses are plotted on the second curve, fig.6.3, and shows that the process is non-adiabatic. It is interesting to recognize the profile seen on the taper test, fig.5.6, emphasizing to some extent that a *PaDo* react as a *STF*.

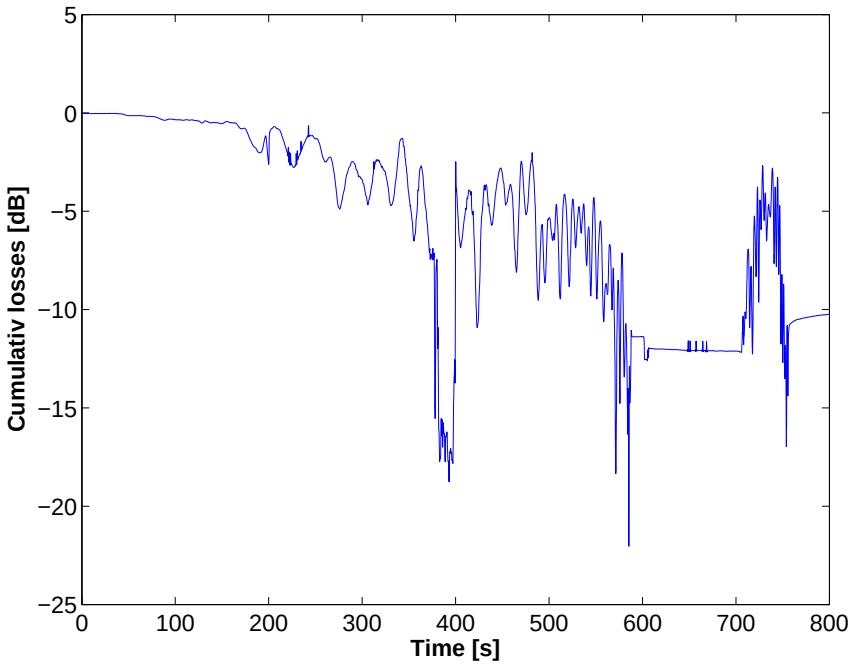

Figure 6.3: Cumulative insertion loss for *Coupler A* as a function of time.

(a)

	straigth arms	cross arms
min	0.13	0.217
max	3.83	1.53
avg	1.73	0.69
stdev	0.95	0.32

(b)

	straigth arms	cross arms
min	0	0
max	0.24	0.13
avg	0.05	0.12
stdev	0.06	0.04

Table 6.2: (a)*PDL* [dB] and (b)*DGD* [ps] for the *Coupler A*

The amount of power lost during the process is non negligible, since the final value is around $10dB$, and that other groups obtain an insertion loss value 2 order below.

Concerning the measured charateristics, only the *PDL* exhibit values far greater than a common optical component. The tables below sum up the values of the *PDL*, tbl.6.1(a), and the *DGD*, tbl.6.1(b), for the straight arms and the cross arms[1].

Thanks to the work made on the taper drawing, the adiabatic program is then used to draw a coupler.

[1]The curves are included in F.1-p.81 and F.2-p.82

6.2 Results with the adiabatic process - *Coupler B*

A great help is found in the work of Suzanne Lacroix's group, and especially on the article [] that contains many useful practical curves, allowing to design a coupler and verify its properties.

6.2.1 Additional fusion stage

Prior to make a coupler, the *PaDo* has to be submitted to an high temperature, so that the fibers start collapsing together. This is the fusing stage.

Suzanne Lacroix's fusing model is used. It shows that two similar fibers can collapse into a single structure, where the cores are separated by a distance d equal to :

$$d = 2(\sqrt{2} - 1)r_{cl}$$

where r_{cl} is the cladding radius. A fusion coefficient is defined as :

$$f = \frac{2r_{cl} - d_{meas}}{2(2 - \sqrt{2})r_{cl}} \tag{6.1}$$

It gives a value of 0 for two adjacent fibers and a value of 1 when the fibers are collapsed to the maximum. To measure this coefficient, it is sufficient to measure the total width D_{meas} of the fused structure, since d_{meas} is related to it through :

$$D_{meas} = d_{meas} + 2r_{cl} \tag{6.2}$$

Combining eq.(6.1) and eq.(6.2), one will obtain :

$$R_{meas} = 2r_{cl} - (2 - \sqrt{(2)}) \cdot f \tag{6.3}$$

According to Suzanne Lacroix's tips, a good fusion ratio is supposed to be 0.8. Some investigations are made with the Vytran machine to realize this fusion operation.

The temperature of the Vytran fiament is set to its maximum, so to say 3000řC with a Tungsten filament, as is the Argon flow to prevent an early oxydation of the *PaDo*. In this configuration, the machine is pushed to its limit and the whole system start to rise in temperature. Moreover, due to the properties of the Tungsten filament, a metal deposit appears on the surface of the fiber. Both reasons lead to reduce the fusion time to its minimum.

The test results are gathered in fig.6.4. They show the fusion coefficient obtained for the *PaDo* with a hot zone of $1cm$. The maximum fusion coefficient obtained has a value of approximately 0.4, and requires a fusion time of 25 minutes. To limit the

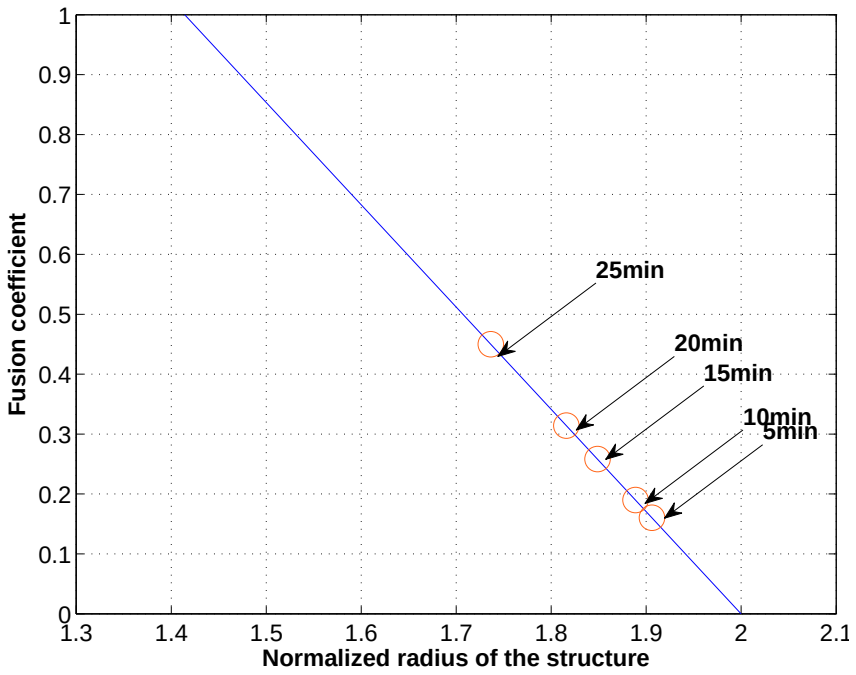

Figure 6.4: Results for the fusion stage. The blue curve is derived from eq.(6.3)**. The orange circles represent the value of the fusion coefficient as measured on the *PaDo*.**

negative effects on the machine and on the fiber, the fusion time is limited to this maximum value of 25 minutes.

Some picture of the *PaDo* are taken after the fusion process. It is interesting to compare the transversal view of the *PaDo* before the fusion, fig.2.5(a), and afer the fusion, fig.6.5(a).

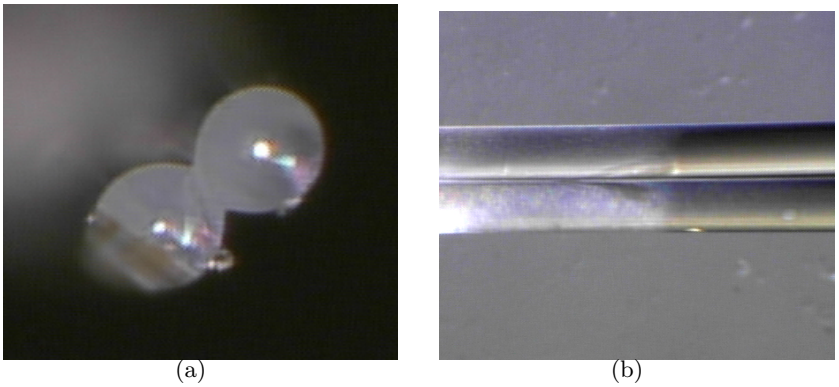

(a) (b)

Figure 6.5: Transversal view (a) and longitudinal view (b) of the *PaDo* after the fusion process. (b) shows the oxidation of the *PaDo*

But also to notice the affected outer surface of the *PaDo*.

6.2.2 Results

Once the fusing stage is done on the *PaDo*, the making of a coupler is performed. The program used is now an evolution of the adiabatic macro.

	T[°C]	$V_{7,8}[\mu m/s]$	$L_{7,8}[\mu m]$	$V_9[\mu m/s]$	$L_9[\mu m]$	$t[s]$
motion 1	3000	0	0	240	$\pm$4000	1500
motion 2	1644	24	3840	240	$\pm$4800	160
motion 3	1543	8	440	240	$\pm$4800	55

Table 6.3: Vytran parameters for the *Coupler B*

The comparative evolution of the transmission in both arms is plotted, fig.6.6. On a overall point of view, the process is much more stable than with the previous parameters.

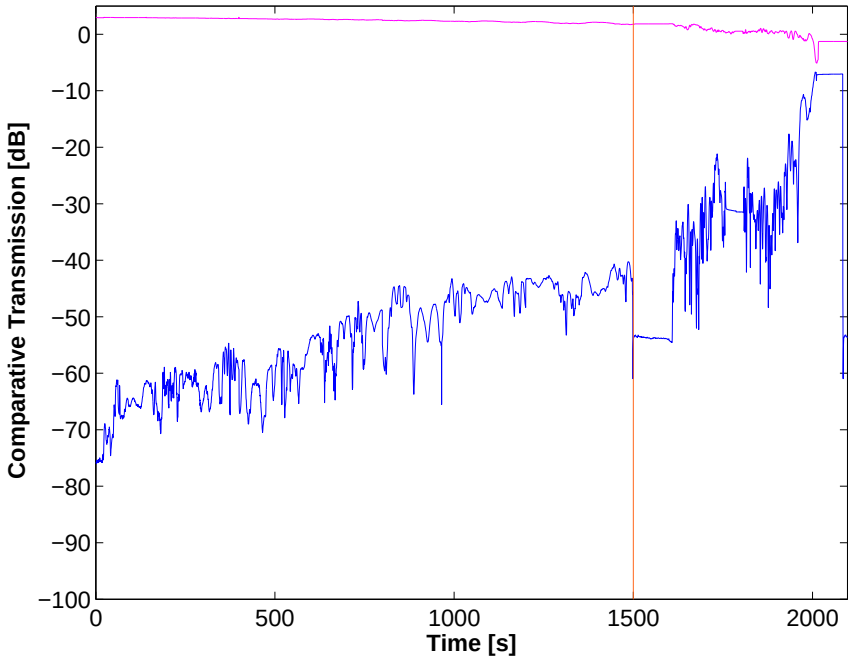

Figure 6.6: Coupling of light in *Coupler B*, cross arm in blue and straight arm in magenta. The vertical orange line states the separation between the heating and pulling stages.

The part before the orange vertical line represent the period when the *PaDo* is heated during the fusing stage. The coupling is already increasing during this fusion stage, rising from almost nothing to $-40dB$. However, it is also accompanied by a rise in the losses, fig.6.7, up to $1dB$.

These early losses are mainly induced by the twisting and stress induce by such a long time at a high temperature. Indeed during the fusion, the fiber is so soft that a slight misalignment between the two fiber holder will induce a irreversible bend on the *PaDo*.

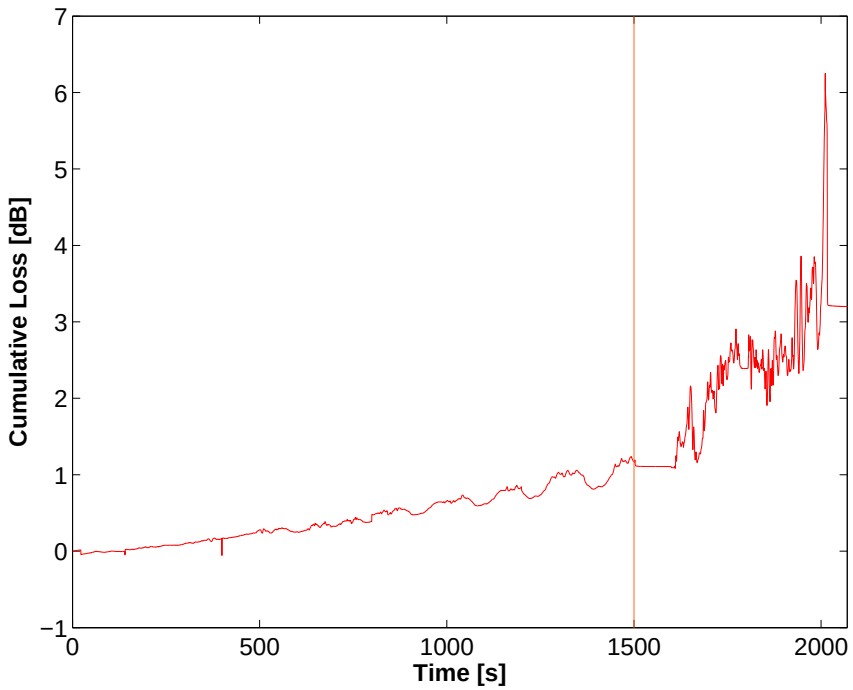

Figure 6.7: Insertion losses in the *Coupler B* as a function of time. The vertical orange line states the separation between the heating and pulling stages.

After the orange vertical line is the pulling stage, fig.6.8 shows a closer look. The evolution is still a bit erratic, and at the time the two curves seems to be crossing, the pulling is stopped. The final tuning is not accurate, more than 50% lower than the target value. But due to manufacturing reasons, it is decided to keep the coupler in this state.

Considering again the losses, fig.6.7 shows that they explode when entering the pulling stage. The electric field is at this time filling up the cladding, and thus feeling to a strong extent the metal deposit on the outer diameter.

An intermediate stage between the fusion and the pulling could be added to remove the metal deposit.

6.2.3 Characteristics of *Coupler B*

Finally, the obtained coupler has the following characteristics. The coupling ratio C_r is equal to 0.22 and the insertion losses are around $3dB$.

The α coefficient of the coupler is derived from (5.3). One will obtain the following relation :

$$\alpha = \frac{\arccos(2 * T_{cross} - 1)}{2} \tag{6.4}$$

and by setting T_{cross} equal to the C_r, one will get $\alpha = 0.4882$, a value close to $\pi/6$.

The *PDL* and the *DGD* are also measured on the coupler[2], tbl.6.4. First, the *PDL* of *Coupler B* is far lower than *Coupler A*, so to say 1 order below for the straight arms, while the *DGD* exhibits similar values. Then, as compared to their initial values, both *PDL* and *DGD* exhibits an increase of only a few precent.

The normalized transverse dimension τ of the coupler is measured to 0.4 ; in concordance with the model which give 0.41. This values lead to an estimate of the normalized wavelength period Λ close to $500nm$, as derived from [15].

These are the properties of *Coupler B*, characteristic of a little melted ($f = 0.4$) and little pulled coupler. The process is stopped when the first half power transfer is reached.

[2]The curves are included in F.1-p.81 and F.2-p.82

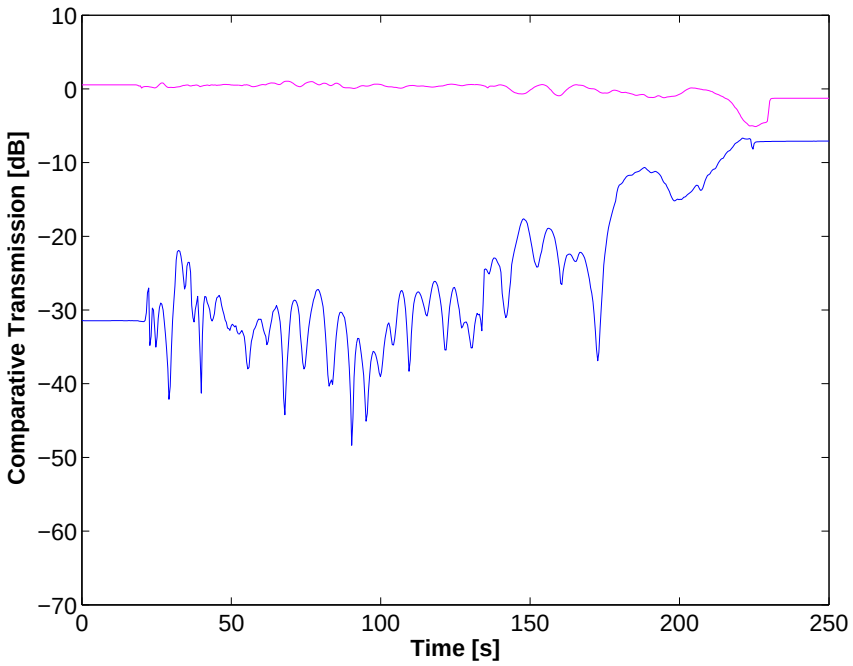

Figure 6.8: Coupling of light in *Coupler A* during the pulling stage, cross arm in blue and straight arm in magenta.

(a)

	straigth arms	cross arms
min	0.019	0.066
max	0.466	0.393
avg	0.195	0.245
stdev	0.116	0.137

(b)

	straigth arms	cross arms
min	0	0
max	0.24	0.13
avg	0.05	0.12
stdev	0.06	0.04

Table 6.4: (a) *PDL* [dB] and (b) *DGD* [ps] for the *Coupler B*

6.3 Conclusion on the coupler making process

The process of making a coupler with the Vytran machine is possible in *PaDo*, according to the result obtained with *Coupler B*.

While the obtained component exhibits a very satisfying *PDL* and *DGD*, the coupling is a constant hard to tune finely. The instability of the setup and the measuring method take account for this problem.

The insertion losses are also from far much higher than what is to be expected. The heating system, based on a resistive filament, is there responsible for an absorbing metallic deposit on the outer diameter of the structure. Moreover, the difficulty to align the fiber in a straight way between the two fiber holders is also responsible for its share.

As a result, one might conclude that the Vytran machine, used as a coupler maker, is a poor choice of device to obtain the desired results.

Considering the losses, an additional work has been led to remove the metal coating. A light etching in *HF* gives a complete removal, to a price of more lab handling of the setup.

Nevertheless, this *Coupler B* has been qualified to build a Michelson interferometer.

Chapter 7

Michelson Interferometer

A coupler is the only component required to build the most simple beam splitting interferometer : the Michelson interferometer.

The in-air setup is shown in fig.7.1. It is composed of a light source (here a laser), a beam splitter and two mirror. The laser beam is split in two equivalent beams, that are mirror-reflected back to the beam splitter, and eventually superposed at the output to produce the non-localized interferences.

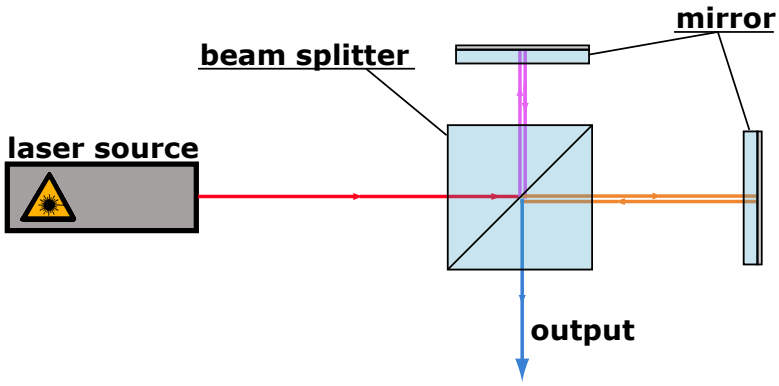

Figure 7.1: In-air Michelson interferometer setup

In the present work, the interferometer is monolithically built in the *PaDo*, fig.7.2. The optical components are replaced by their equivalent in the fiber optics field. A coupler is used as a beam splitter, and the 4% reflection at the glass/air interface is used as a mirror.

7.1 All-in Michelson interferometer

The setup is composed of the left side of the previous setup, fig.5.3. Two pigtails connect the input and the output of the interferometer. $60cm$ of *PaDo* is reserved

after the *Coupler B* and constitute the arms of the interferometer. Finally a cleave on the *PaDo* creates the mirrors in both arms.

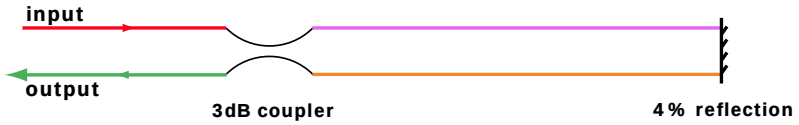

Figure 7.2: In-fiber Michelson interferometer setup

Considering the losses in the setup, namely the $3dB$ insertion loss of the *Coupler B* and the $14dB$ of the mirrors, the light source of the *OSA* is not suitable to perform the measurement. The level of noise is comparable to the signal level. A *S-LED* is used instead. It provides a comfortable input power over a wide bandwidth.

7.2 Theoritical expectations

A mathematical modeling is used to predict the results.

One hypothesis is made. Considering the normalized wavelength of the coupler Λ equal to approximately $500nm$, the coupling is supposed to be flat in the region of interest. The variation of α with regards to the wavelength is linear, and approximated here to be null.

Using the matrix formalism, the interferometer is modeled as a *MZI*. It is unfolded in two couplers separated by a propagating medium. This medium introduce a relative phase shift φ modeling unbalanced arms, an extra π*-shift* accounting for the inner reflection on the mirrors and an attenuation coefficient A for the insertion losses.

The transfer matrix of the system $T_m(\alpha)$ is given by, according to (5.1):

$$T_m(\alpha,\varphi) = T_{2*2}(\alpha)\begin{bmatrix} A\exp(i\varphi) & 0 \\ 0 & A \end{bmatrix} T_{2*2}(\alpha) \tag{7.1}$$

with φ equal to $\kappa z + \pi$ or $2\pi\delta d/\lambda + \pi$, and δd the arm mismatch.

This finally leads to the expression of the power transmission :

$$T_2(\alpha,\varphi) = \frac{A}{2}(1-\cos^2(2\alpha)+\sin^2(2\alpha)\cos(\varphi))$$

or equivalently :

$$T_2(\alpha,\varphi) = \frac{A\sin^2(2\alpha)}{2}(1+\cos(\varphi)) \tag{7.2}$$

in which the computed value of α can be used.

7.3 Results

The Michelson interferometer is characterized, fig.7.3. This measure is rather difficult to obtain due to the instability of the setup. The *Coupler B* is taken off the Vytran machine and taped on an aluminum plate. However, it is hard to reproduce the conditions in which it was when made (tension, alignement, ...). As a results, its characteristics are fluctuating until a nice tuning is found.

Several measurement are made. The arms of the interferometers are extended straight to minimize the differential light path, and obtain the maximal free spectral range (FSR). One measure is shown on fig.7.3 and exhibits interesting properties.

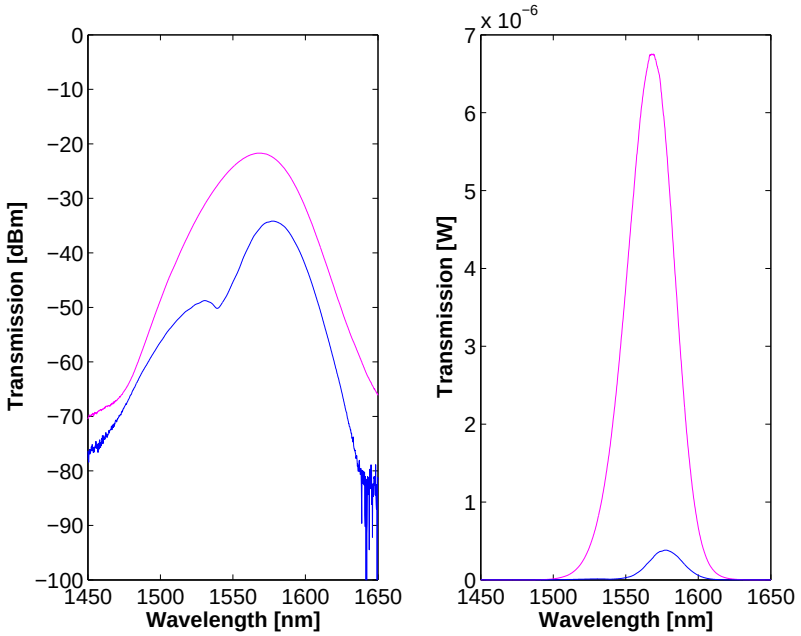

Figure 7.3: Comparative transmission of the light source (magenta) and the cross arm of the Michelson interferometer (blue), in logarithmic and linear scale.

The linear measurement is confronted to the modeled curve from (7.2), see fig.7.4. The fit is conclusive according to the period of the beating, even if the power level exhibits a deviation from the prediction.

The main point in this curve is the huge FSR of $110nm$ obtained with the *PaDo*. This result has to be compared with previous showing usually a value two order of magnitude lower, in the vicinity of $1nm$.

Using the derivative of the phase shift φ reveals the arm mismatch :

$$\delta d = \frac{n}{2}\frac{\lambda_1\lambda_2}{\lambda_2 - \lambda_1} \approx 10.77\mu m$$

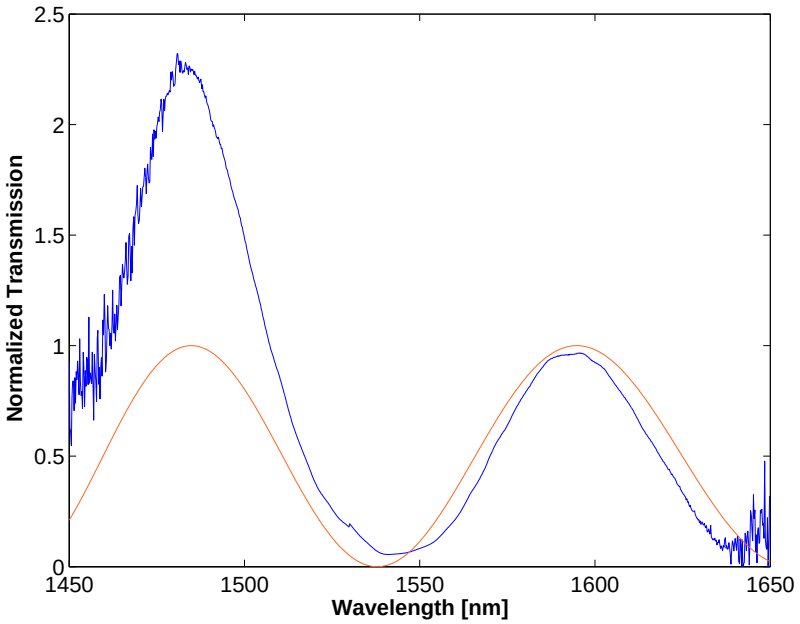

Figure 7.4: Measured transmission in the cross arm of the Michelson interferometer, compared with the simulation.

with $\lambda_1 = 1485nm$, $\lambda_1 = 1595nm$ and $n = 1$.

The likeness of the halves allows to obtain such a small differential light path, leading to a great *FSR*. Moreover, this spectrum is shown to be stable in time.

7.4 Conclusion

Comparing the results obtained with other groups shows that the use of *PaDo* is capable of major benefits in balancing the arms of an interferometer. It suppresses the need of a polarization control of the inputs and provides a stability in time and temperature.

As a result, the *PaDo* is proven to be highly suitable in the production of a balanced interferometer, taking advantages of its special geometry.

Chapter 8

Fiber Bragg Gratings

8.1 Introduction

Acreo's state-of-the-art fiber Bragg grating (*FBG*) facility is used to produce *FBG* on *PaDo*.

FBG can be assimilated to wavelength selective filter. Their periodical variation of effective refractive index leads to the interference phenomena through multiple reflections. For a certain range of wavelength, those reflections will induce constructive interference in reflection. The transmitted field is thus filtered out of those wavelengths.

Producing those grating requires the inducement of a periodical variations of the fiber core index. It is a two step process. First, the fiber is made light sensitive by being submitted to a high pressure hydrogen loaded atmosphere. The hydrogen is slowly diffusing in the fiber core, several days are required to assure a sufficient hydrogen loading. Then, the sinusoidal interference pattern of a strong laser beam expose the fiber core, that will react to the light by an increase in refractive index, in proportion to the intensity received.

The mathematical description of the light behavior in such a structure is easily found in the literature[16]. Nevertheless the simulated reflectivity as a function of wavelength is shown in fig.8.1.

With regard to the induced periodical refractive index in the fiber, one can tune the properties of the *FBG*'s reflective profile. So to say, apodized profile will reduce the sidelobs intensity, or chirped profile will broaden the spectrum ...

As a constitutive part of an *ADM*, *FBG* writing is studied on *PaDo*.

8.2 Results of *FBG* with *PaDo*

The first task is to assure that a writing in one half will not affect the other half, and *FBG*s written in both halves are equivalent, fig.8.2.

The first test shows that the writing of one fiber does not affect the other, but the reflectivity profile is not equivalent on both fibers. This comes from the alignment

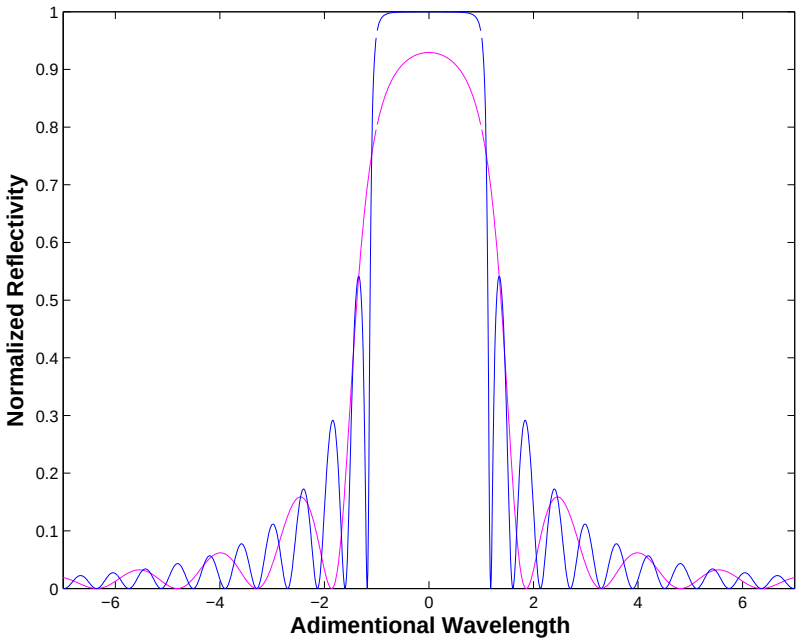

Figure 8.1: Simulated reflectivity of a *FBG* with two different strenght

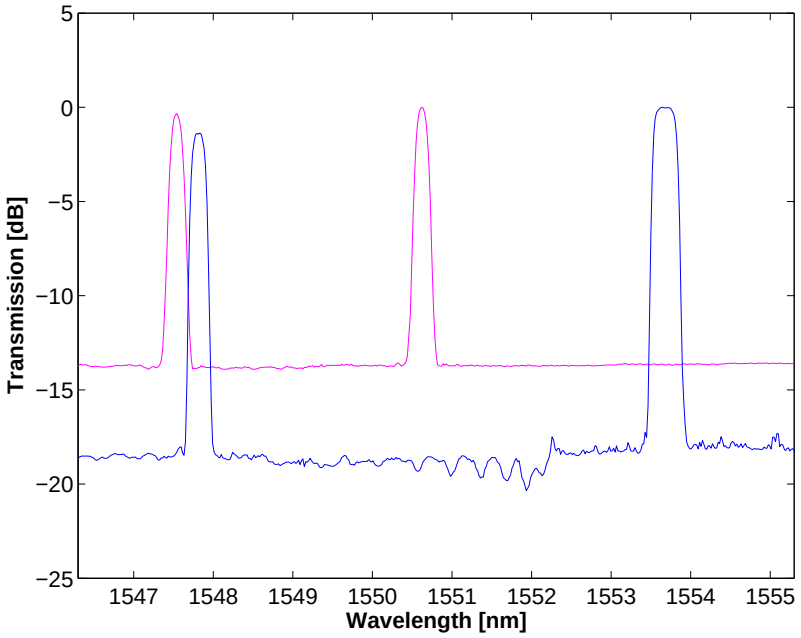

Figure 8.2: Test of *FBG* writing on *PaDo*. With the regular fiber holders, both halves exhibits different writings.

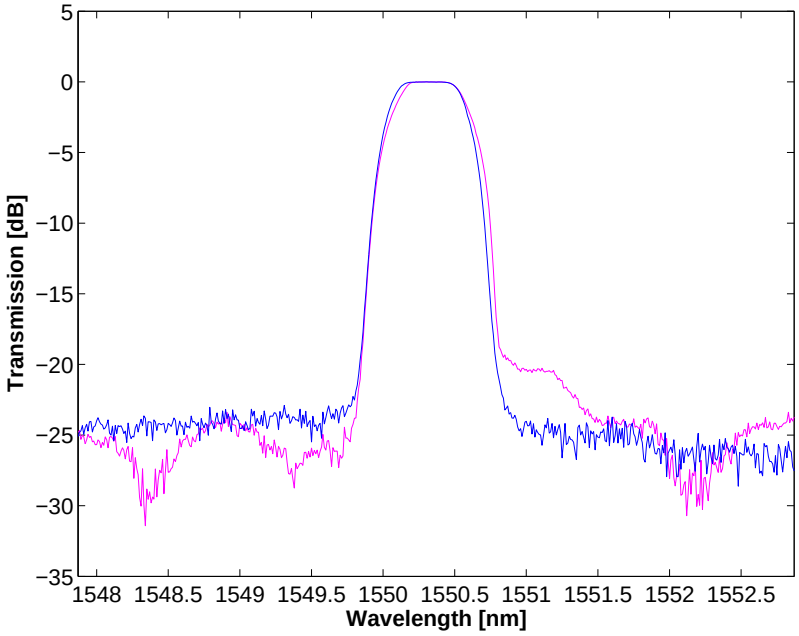

Figure 8.3: Equivalent *FBG*s in both halves of a *PaDo*

procedure in the machine : one half was further form the focal plane than the other, experiencing a longer period in the interference pattern of the writing laser beam.

New fiber holders have been produced and give a very satisfying result, fig.8.3.

A quick experience is led on this setup. A longitudinal bending is applied to the *PaDo* on the region where the *FBG*s are written. As a result, the *FBG* in the inner part of the bend will be compressed while the other one will be extended. The expected and verified results is a shift of the reflective spectrum to lower wavelength for the inner *FBG* while the outer *FBG* will present a spectrum shifted to longer wavelength, fig.8.4.

The amount of relative shift in this experience is measured to be around $1nm$, but later work achieves some $4nm$ until the limit of *PaDo*s mechanical resistance is reached.

8.3 Conclusion

The writing of *FBG* in *PaDo* is shown as feasible as in common *STF*. The obtained results exhibits the same quality standards, and the tuned fiber holders allow to use the *PaDo* in the exact same way.

Moreover, the use of *PaDo* opens the way to a new sensor technology. The idea is to monitored two quantities at a time. For example, pressure and temperature can be measured with twins *FBG* in a *PaDo*. A change in temperature will lead to a shift in the reflective spectrum for both *FBG*, while an induced pressure along

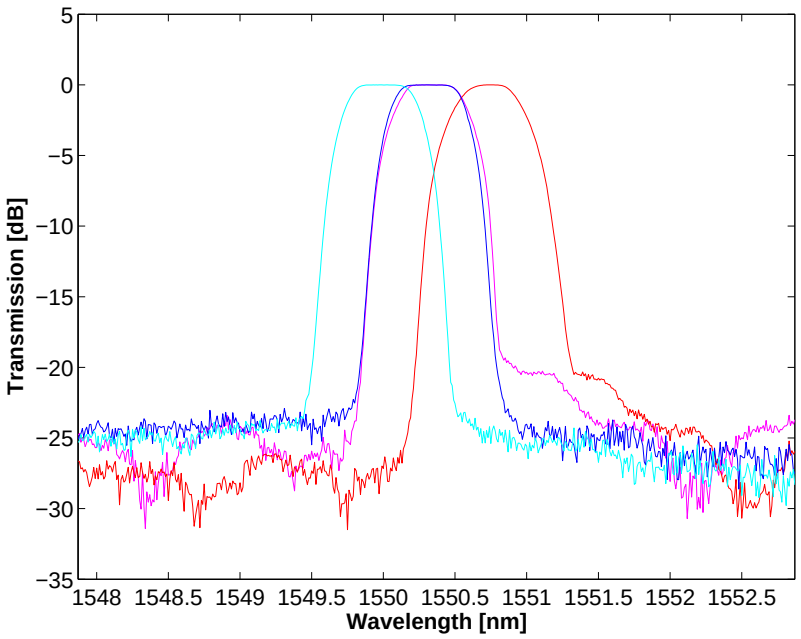

Figure 8.4: Bending of *FBG* written *PaDo*, and effect on the *FBG*'s spectrums

the transversal dimension will induce an opposite shift in both *FBG*.

This new design is one the possibilities offered by the special geometry of the *PaDo*.

Chapter 9

Conclusion

Some general conclusion can be drawn from this work.

The *PaDo* and *PaDowH* have been handled with success in the task of connecting the fibers tip. The reproducible and low-loss process is defined and mastered.

The characterization of *PaDo* and *PaDowH* have underlined the quality of those fibers by the mean of their *PDL* and *DGD*. They are shown usable to make optical components based on *MZI*.

The taper structure and by extension the coupler component have been of extensive study in this work since they revealed themselves more complicated to build than expected.

Both structure have been achieved, but the processes remain to be improved. Some leading ideas have been advanced to lower the insertion losses, the next step being to master more accurately the coupling ratio of the produced coupler.

The writing of *FBG* in the *PaDo* has also been validated. It shows exciting results about sensors capabilities for these fibers.

On a larger extent, if building a *MZI* structure in the *PaDo* has not been achieved, the results obtained with the Michelson interferometer are extremely encouraging towards this goal. The special *PaDo* geometry provides as expected a huge *FSR*, around $110nm$ or two order of magnitude better than with standard fibers, but also an input polarization independence and a great time/temperature stability.

Finally, my work here in Acreo as covered a period of 6 month during which I had the pleasure to be part of a research team, from the Fiber Component Lab, in a company that positions itself at the point where research and industry are merging.

This experience is from far the more interesting in my beginning engineer life and will be a good starting point to pursue my way in the work environment.

Bibliography

[1] Eugene Hecht. *Optics*. Pearson Education, 2005.

[2] Wikipedia. Michelson morley experiment - wikipedia.

[3] K. Okamoto. Theoretical investigation of light coupling phenomena in wavelength-flattened couplers. *Journal of Lightwave Technology*, 8(5):678–682, 1990.

[4] M. Fokine, L. E. Nilsson, Å. Claesson, D. Berlemont, L. Kjellberg, L. Krummenacher, and W. Margulis. Integrated fiber mach-zehnder interferometer for electro-optic switching. *Optics Letter*, 27(18):1643–1645, September 2002.

[5] Hania Arsalane. Inducing refractive index changes in internal electrodes fibres. Master's thesis, Ecole Nationale Supérieure de Physique de Marseille, 2001.

[6] Acreo webpage.

[7] I. Yokohama, J. Noda, and K. Okamoto. Fiber-coupler fabrication with automatic fusion-elongation processes for low excess loss and high coupling-ratio accuracy. *Journal of Lightwave Technology*, LT-5(7):910–915, July 1987.

[8] Y. Takeuchi and J. Noda. Novel fiber coupler tapering process using a microheater. *IEEE Photonics Technology Letters*, 4(5):465–467, 1992.

[9] T.E. Dimmick, G. Kakarantzas, T.A. Birks, and P.St.J. Russel. Carbon dioxide laser fabrication of fused-fiber couplers and tapers. *Applied Optics*, 38(33):6845–6848, 1999.

[10] C. McAtamney, A. Cronin, R. Sherlock, G. M. O'Connor, and T. J. Glynn. Reproducible method for fabricating fused biconical tapered couplers using a co2 laser based process. In *Proceedings of the Third International WLT-Conference on Lasers in Manufacturing 2005*, 2005.

[11] Charles Jewart, Kevin P. Chen, Ben McMillen, Michael M. Bails, and Steven P. Levitan. Sensitivity enhancement of fiber bragg gratings to transverse stress by using microstructural fibers. *Optics Letter*, 31(15):2260–2262, August 2006.

[12] Craig D. Poole and David L. Favin. Polarization-mode dispersion measurements based polarization-mode dispersion measurements based on transmission spectra through a polarizer. *Journal of Lightwave Technology*, 12(6):917–929, june 2004.

[13] J.D. Love, W.M. Henry, W.J. Stewart, R.J. Black, S. Lacroix, and F. Gonthier. Tapered single-mode fiber and devices - adiabaticity criteria. *Optoelectronics*, 138:343–354, 1991.

[14] S. Lacroix, J. Bures, and J. Lapierre. Analyse d'un coupleur bidirectionnel à fibres optiques monomodes fusionnees. *Applied Optics*, 22(12):1918–1922, 1983.

[15] Suzanne Lacroix, Frangois Gonthier, and Jacques Bures. Modeling of symmetric 2 x 2 fused-fiber couplers. *Applied Optics*, 33(36):8361–8369, December 1994.

[16] Amnon Yariv. *Quantum Electronics*. John Wiley and Sons, 1988.

[17] D.T. Cassidy, D.C. Johnson, and K.O. Hill. Wavelength-dependant transmission of monomode optical fiber tapers. *Applied Optics*, 24(7):945–950, 1985.

[18] F. Gonthier. *Conception et réalisation de coupleurs multifibres intégrés à des fibres optiques unimodales*. PhD thesis, Ecole Polytechnique de Montréal, 1993.

[19] Timothy A. Birks and Youwei W. Li. The shape of fiber tapers. *Journal of Lightwave Technology*, 10(4):432–438, 1992.

[20] Govind P. Agrawal. *Fiber-Optic Communication Systems*. John Wiley and Sons, 1997.

Appendix A

Fabry-Perot interferometer

The opportunity to develop a Fabry-Pérot interferometer (*FPI*) has been given by an adjunct project, an optical fiber based positioning system. The fiber is used as a probe, it shines the studied surface with a broad source and records the reflections. This device uses the interference phenomenon between the reflected wave of the fiber tip and the reflected wave of the surface in order to compute the length between the fiber tip and the surface. A *FPI* etalon is wished to characterized the whole setup in a set and known case.

The novel FPI building process is presented. The main idea relies on the utilization of a fiber capillarity that encloses the cavity made by two cleaved *STF* tips. It exhibits several advantages :

- the structure is stable in time, in the order of the μm.
- the length of the cavity can be tuned during the process with a precision of $1\mu m$.
- performances of $14.5dB$ for extinction ratio and $0.6dB$ for insertion loss are achieved with uncoated STF tips.

A.1 Setup

The physical scheme of this setup remains very simple to build, fig.A.1, and exhibits the advantage to be embedded in the fiber. First, the fibers are introduced into a $129\mu m$-core capillary and pushed in contact. This structure is placed on the Vytran machine, with the fiber holders on both sides. One side is fixed by melting the capillary against the fiber. Then, the cavity is formed by pulling the left free fiber with the step motor controlled fiber holder. The cavity consists of air between to the two cleaved STFs tips, maintained together by the capillary. Finally, once the desired length d of the cavity is reached, the second side of the structure is closed by melting the capillary against the fiber.

The gap region has been observed under a microscope, fig.A.2. A STF is place in regard to the gap to give an account of its width.

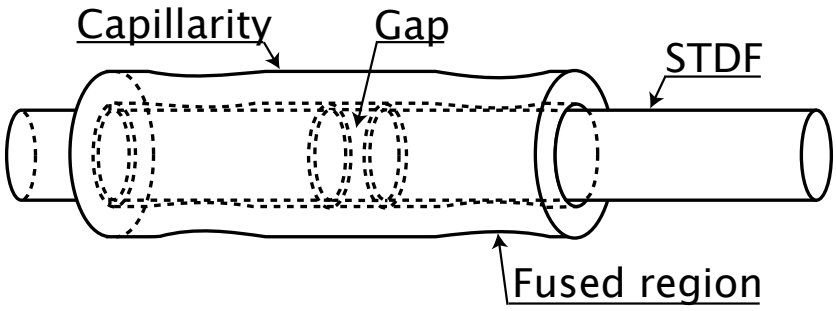

Figure A.1: Setup of the FPI

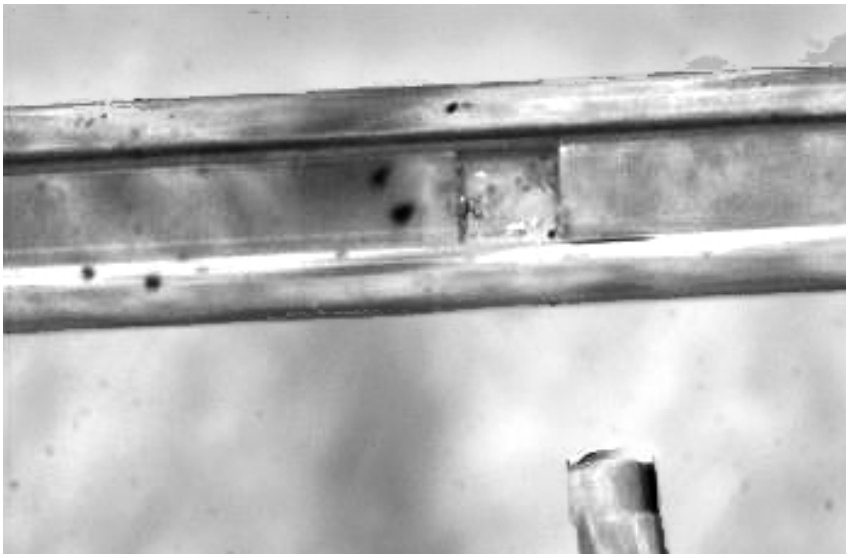

Figure A.2: FPI seen through microscope

The length d of the cavity is tunable within a wide range, from several to hundreds μm.

A.2 Theory and expectations

The FPI dealt with here is studied in reflection, even if the setup allows to use it in transmission. According to literacy[1], the quotient of the reflected intensity over the input intensity is :

$$\frac{I_r}{I_o} = \frac{F \sin^2(\delta/2)}{1 + F \sin^2(\delta/2)}$$

where F is the so-called finesse, r is the reflection coefficient from the STF core

to the gap, and δ the phase-shift between to consecutive rays. These quantities are defined by :

$$F \equiv \left(\frac{2r}{1-r^2}\right)^2 \qquad r = \frac{n_i - n_t}{n_i + n_t} \qquad \delta = \frac{2\pi}{\lambda} n_i 2d$$

In this case, the approximation of normal incidence is made, and the refractive indices are $n_i = 1.45$ and $n_t = 1.0$. The fig.A.3 and fig.A.4 shows the theoretical curves of the reflectivity versus δ for three value of the finesse, and the evolution of the finesse with regards to the reflection coefficient.

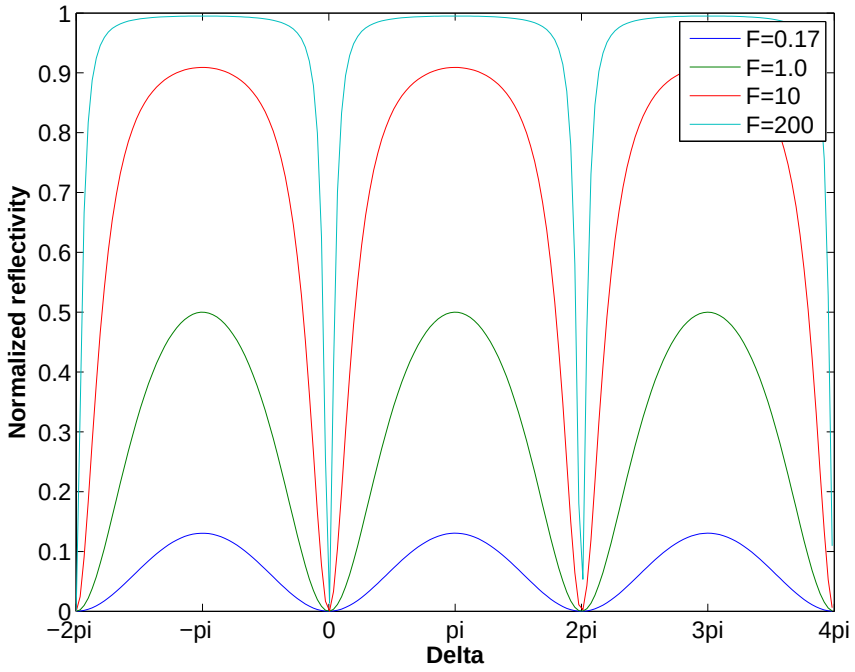

Figure A.3: Theoritical curve of the Reflectivity with regards to the phase-shift.

A.3 Results

The measurement is made with an OSA and a laser source from Ando and a circulator. As expected from the simulation, oscillations are recorded in the cavity, fig.A.5.

The attenuation is around $0.6dB$ as compared with the simulation. That can be explain by the approximation made : no-loss mirror and normal incidence. Moreover some pieces of glass are trapped into the gap, constituting scattering sites. The same reasons are responsible for a maximum extinction ratio is of $14.5dB$.

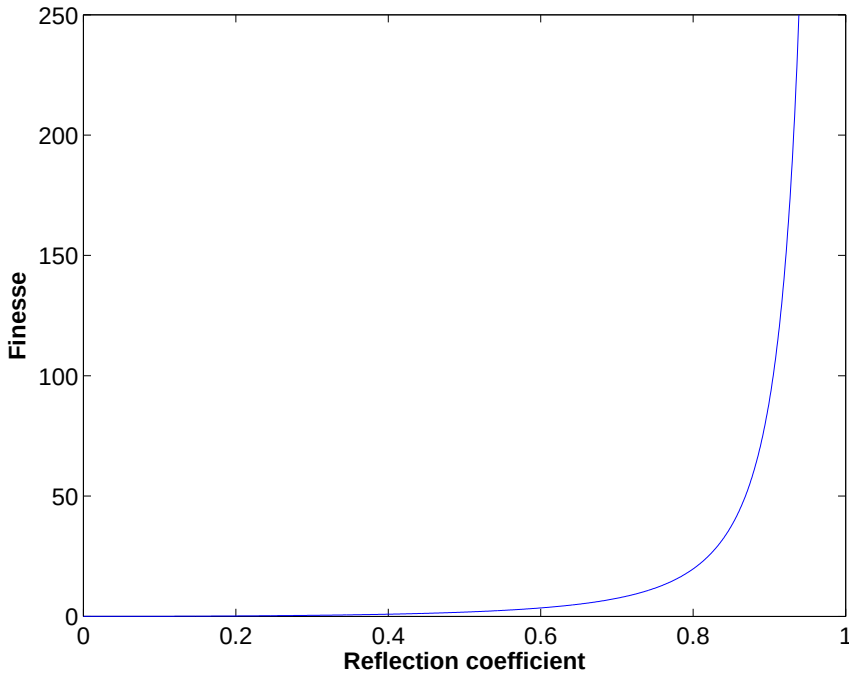

Figure A.4: Theoritical curve of the Finesse with regards to the Reflection coefficient.

The length is computed using a two points method. The following relation hold true for the two datapoints separated by n oscillations, and whose wavelengths are λ_1 and λ_2 :

$$2\pi 2d\frac{\lambda_2 - \lambda_1}{\lambda_1\lambda_2} = 2n\pi$$

or equivalently :

$$d = \frac{n}{2}\frac{\lambda_1\lambda_2}{\lambda_2 - \lambda_1}$$

The value for the cavity is computed to be $55.7\mu m$ and is consistent with the simulation. Moreover, the curves in blue represent measurement taken over several days and exhibits a good stability.

The curves with a logarithmic scale, fig.A.6, shows a good view of the losses. The insertion loss is relatively low, while the extinction ratio is dramatically lower than the simulated value. The approximation of normal incidence and perfect mirrors is here showing its limits.

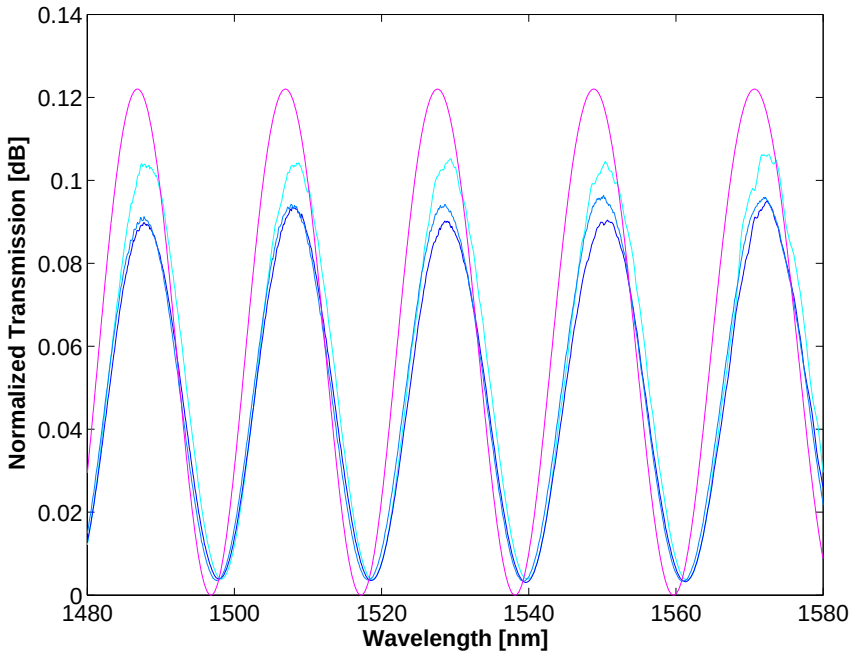

Figure A.5: Comparison between simulated (in magenta), and measured performances (in blue), for measurements over several days.

A.4 Improvements

An additional reflection coating on the fiber tip will increase the finesse of the Fabry Pérot, and then lead to a smaller insertion loss and a better extinction ratio.

Moreover, the recorded curves and the simulation exhibit a small phase-shift. The cleaving angle of the fiber tips is responsible of a beating in the cavity that isn't a multiple of 2π, leading to an absolute error in the measurement. The last figure shows the trend of this deviation, fig.A.7, and as one can guess, the longer the cavity is the bigger the deviation gets.

To improve this, a capillarity with smaller inner diameter can be used to provide a better alignment of the fibers, as will a coated fiber with a high precision cleave.

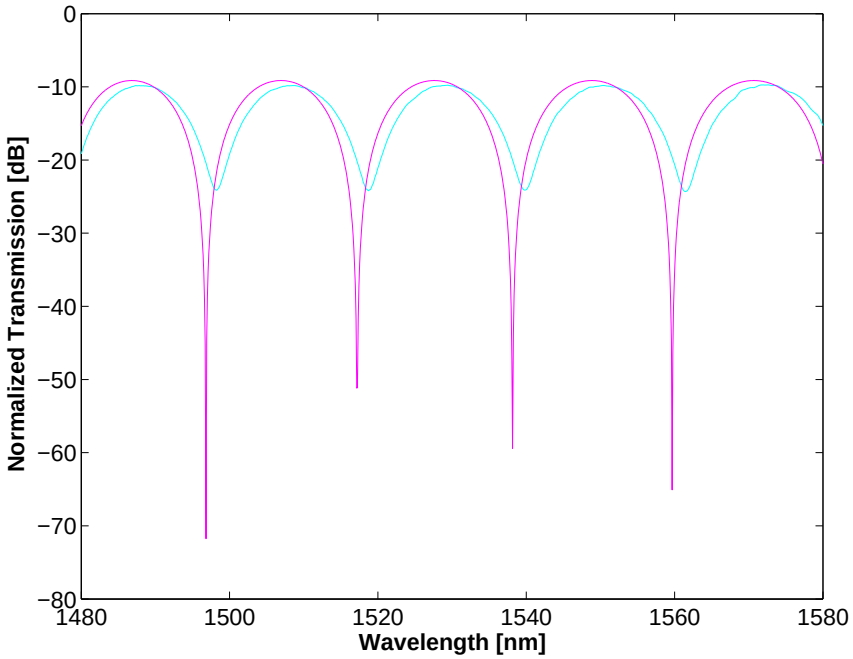

Figure A.6: Comparison between simulated (in blue) and measured (in green) performances.

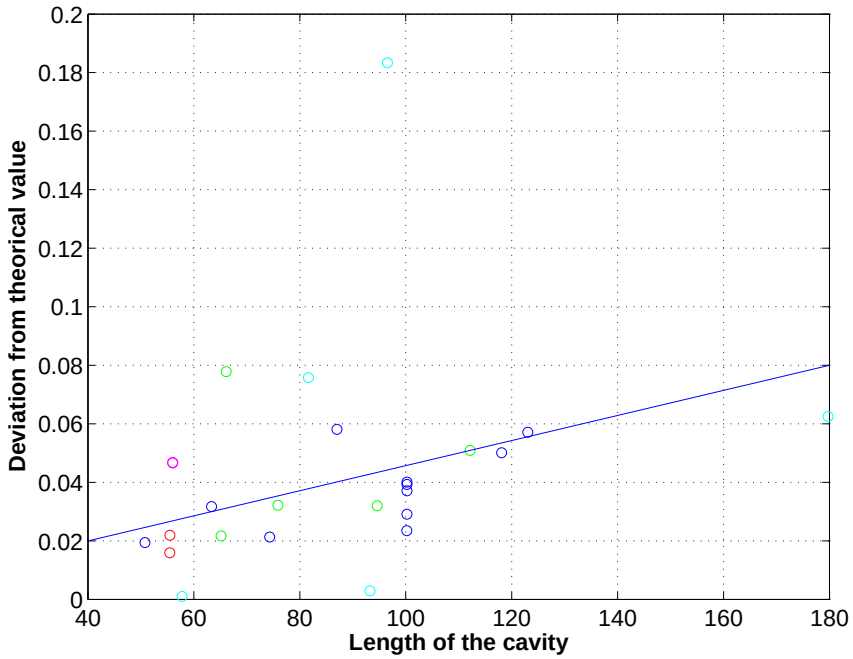

Figure A.7: Deviation of the computed cavity length to the theoretical value with regards to the cavity length.

Appendix B

Misceallenous

STF	Standard Telecom Fiber
PaDo	Paso Doble
PaDowH	Paso Doble with Holes
DCM	Dichloromethane
PDL	Polarization Dependant Loss
DGD	Differential Group Delay
MZI	Mach-Zehnder interferometer
FPI	Fabry-Pérot interferometer
ADM	Add/Drop multiplexer
FBG	fiber Bragg grating
RTC	Real Time Control
DAC	Digital Analog Converter

Table B.1: Table of abbreviations

4	filament DAC
5	Argon flow DAC
7	Left Fiber holder step motor
8	Right Fiber holder step motor
9	Filament step motor

Table B.2: Table of Vytran device ID

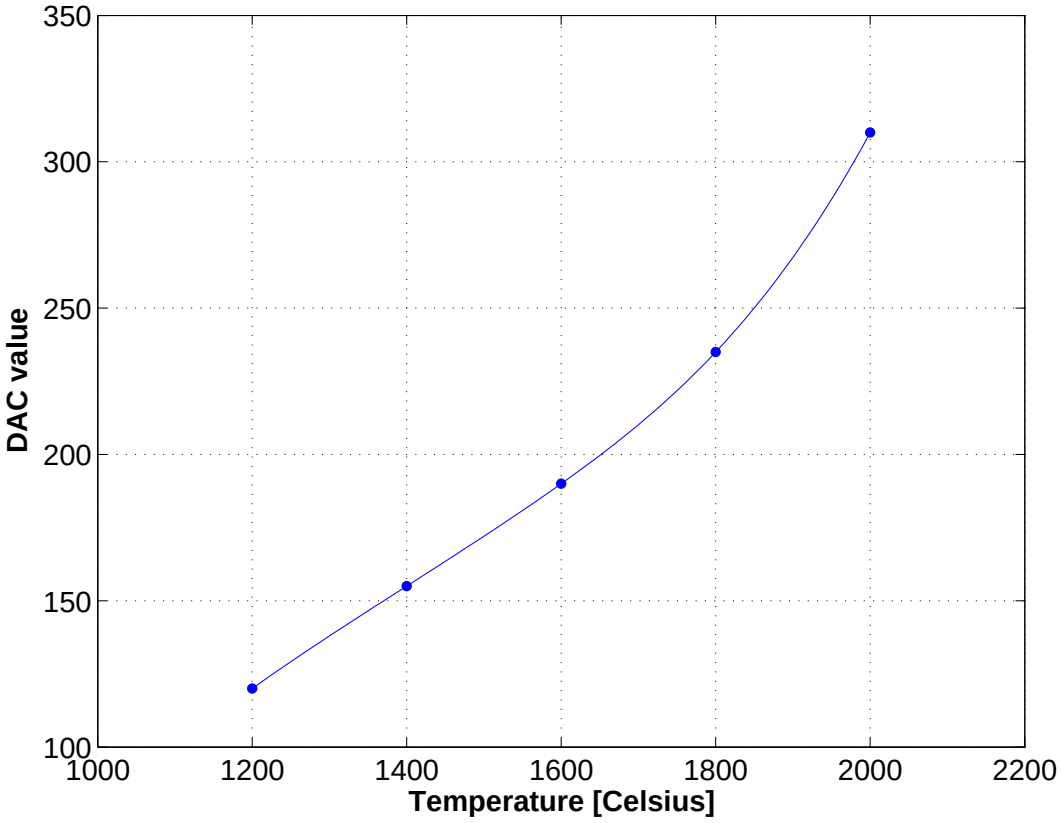

Figure B.1: Calibration curve between the Vytran DAC value and the Iridium filament temperature.

DAC range	linear coefficient - a[V/°C]	linear coefficient - b[V]
155-190	0.175	-90
190-235	0.225	-170

Table B.3: Linear coefficients for the Iridium temperature curve, accounting for $DAC[V] = a * T[\text{°C}] + b$**.**

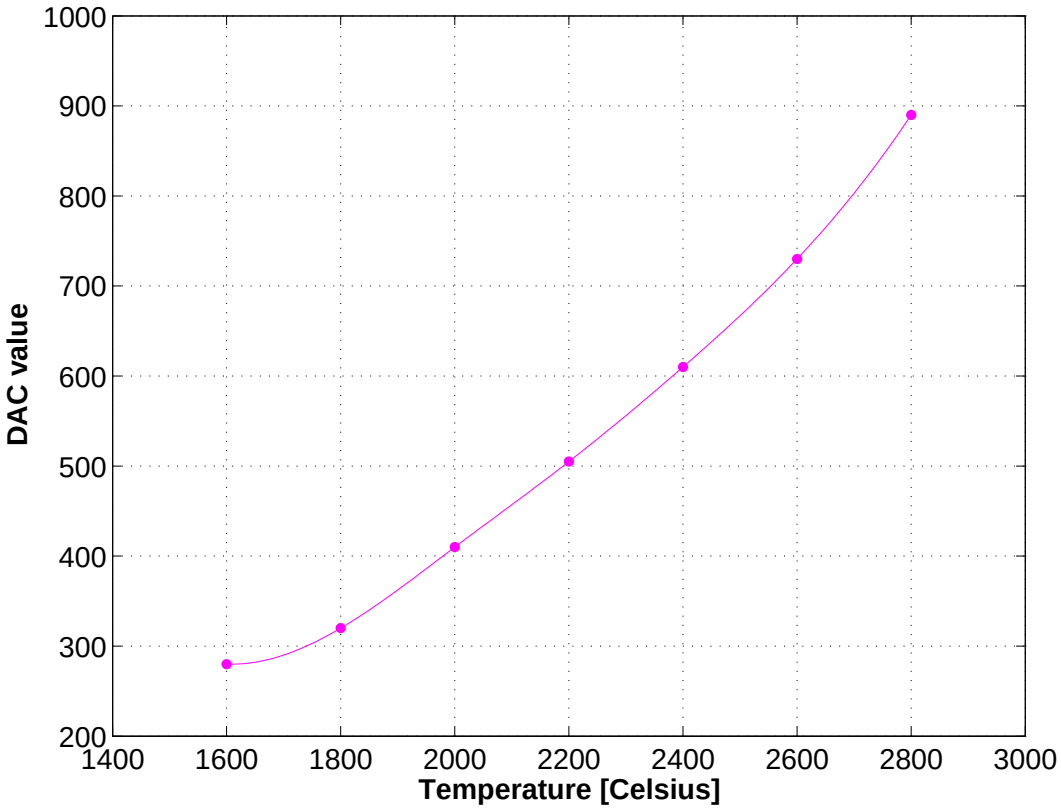

Figure B.2: Calibration curve between the Vytran DAC value and the Tungsten filament temperature.

view angle		gap angle		dB	n°
left	right	left	right	loss	try
0.49	-0.36	1.26	0.88	0.13	2
0.35	-0.53	3.51	0.66	0.29	1
0.71	-0.41	3.32	0.52	x	x
0.23	-0.58	0.37	0.77	x	x
0.3	-0.58	2.04	0.01	0.25	2
0.13	-1.09	0.96	0.77	x	x
0.05	-0.61	0.53	0.58	x	x
0.04	-0.77	1.67	0.8	x	x
0.49	-0.34	1.04	0.78	x	x
0.14	-0.88	1.7	0.64	0.37	1
0.5	-0.83	3.1	0.33	x	x
-0.03	-0.92	2.9	0.88	0.15	1
0.3	-0.65	0.6	1.08	x	x
0.38	0.59	1.14	0.44	0.45	1
0.62	-0.72	2.65	0.14	0.83	1
0.51	-0.54	4.29	0.64	x	x
0.29	-0.68	0.77	0.74	0.5	1
0.54	-0.52	4.31	0.46	x	x
0.55	-0.66	0.94	0.48	0.93	1
0.58	-0.72	0.71	0.67	0.98	1
0.23	-0.51	2.15	0.66	x	x
0.3	-0.31	3.2	0.37	0.79	1
0.5	-0.47	2.69	0.86	1.3	1
0.46	-0.62	1.39	0.57	1.67	1
0.52	-0.59	0.95	0.3	0.69	1
0.21	-0.67	1.76	0.04	0.28	1
0.23	-0.64	2.29	0.76	1.22	1
0.33	-0.62	4.52	0.3	0.19	1
0.46	-0.39	1.43	1.19	x	x
0.2	-0.66	3.59	0.29	0.25	1
0.39	-0.19	1.25	0.24	x	x
0.38	-0.32	0.25	0.45	0.18	1
0.41	-0.38	0.83	0.26	x	x
0.43	-0.34	2.02	1.32	0.11	1
0.14	-0.37	0.45	0.67	0.97	1
0.46	-0.38	0.6	0.27	x	x
0.61	-0.43	0.64	1.25	x	x
0.55	-0.4	0.48	0.79	x	x
0.35	-0.42	1.12	1.35	x	x
0.32	-0.42	5.07	0.47	x	x
0.23	-0.14	0.46	2.74	x	x
0.32	-0.28	0.51	0.74	x	x

view angle		gap angle		dB	n°
left	right	left	right	loss	try
0.27	-0.22	0.34	0.23	0.58	1
0.29	-0.58	0.8	0.25	0.51	1
0.17	-0.51	0.84	1.19	x	x
0.2	-0.74	0.92	0.33	0.2	1
0.43	-0.38	2.98	0.46	0.28	1
0.27	-0.26	1.58	0.43	0.5	1
0.29	-0.42	2.92	0.36	0.31	2
0.52	-1.02	2.2	0.06	1.18	1
0.83	-0.94	0.94	0.42	0.36	1
0.36	-0.8	0.68	0.63	x	x
0.32	-0.31	3.84	0.49	x	x
0.27	-0.79	1.09	0.63	x	x
0.91	-1.09	0.29	0.85	0.84	1
0.74	-1.01	2.95	0.19	0.2	1
0.28	-0.3	2.18	0.62	0.44	1
0.47	-0.7	1.07	1.72	0.18	1
0.68	-0.54	0.08	1.09	0.5	1
0.24	-0.26	3.61	0.32	x	x
0.22	-0.3	1.28	1.58	x	x
0.3	-0.67	2.11	2.76	0.21	1
0.5	-0.31	1.42	0.58	0.05	1
0.17	-0.55	0.39	0.71	x	x
0.19	-0.65	0.69	0.97	x	x
0	-0.36	1.6	1.41	x	x
0.03	-0.32	1.52	1.47	x	x
0.65	-0.34	0.41	2.4	0.25	1
0.33	-0.18	2.36	1.09	x	x
-0.11	-0.36	0.97	0.79	x	x

Table B.4: Measured value for the splicing process n°2

Appendix C

Taper reference program

```
macrobegin(5)

; Filament/Argon initialisation
enablefilament(0)10                    ;disable filament
setdac(4 2500)20                       ;Ar flow (1 l/min)
setdac(5 0)30                          ;no current
macropause(0 2000)40                   ;wait 2 sec

; Motors initialisation
motordatum(7 0)10                      ;set LM position to 0
motordatum(8 0)20                      ;set RM position to 0
motordatum(9 0)30                      ;set CM position to 0

setmotortoggle(7 0)40                  ;LM no toggle
setmotortoggle(8 0)50                  ;RM no toggle
setmotortoggle(9 1)60                  ;CM toggle

macropause(0 100)90                    ;wait 0.1 sec

; Temperature slope increase
enablefilament(1)10                    ;enable filament
setdac(5 50)20                         ;slope
setdac(5 100)500                       ; +
setdac(5 150)1000                      ; ++
setdac(5 180)1250                      ; ++
setdac(5 200)1250                      ; +++
macropause (0 1000)1500                ;wait 1 sec

; Motion 1
motorvel(7 20)10                       ;LM velocity to 20stp/s
motorvel(8 20)20                       ;RM velocity to 20stp/s
motorvel(9 2000)30                     ;CM velocity to 2000stp/s
setdac(5 180)40                        ;motion temperature
motorlimits(9 -2000 2000)50            ;hot zone length

motorexstep(7 -1000000)60              ;LM motion to inf.
motorexstep(8 1000000)70               ;RM motion to inf.
```

```
motorexstep(9 1000000)80                ;CM motion to inf.
macropause(0 400000)90                  ;wait 400s

; Finish section
setdac(5 150)800                        ;Filament down
setdac(5 0)1400                         ;Filament off
setdac(4 300)1410                       ;Argon flow down - background

; Fiber re-tension
motorexstep(7 -20)1430                  ;LM to 20stp
motorexstep(8 20)1440                   ;RM to 20stp
motorto(9 0)1450                        ;CM to 0
macropause(0x1D 10000)1460              ;wait left motor or 10s

;re-init
motorstop(7)10                          ;LM stop
motorstop(8)20                          ;RM stop
motorstop(9)30                          ;CM stop
macroend()
```

Appendix D

Matlab source code

D.1 Data extraction from an OSA measurement file

```
% Filling of structure from OPA Measurement
function [M] = ReadMeasurementOSA(Filename)

fid = fopen(Filename,'r');

if (fid>0)
% reading of data points
fscanf(fid,'%s',2);
M.WLpoints = fscanf(fid,'%f, %f',[2,inf]);

% reading of WL settings
fscanf(fid,'%[^,]',1);
M.WLcenter = fscanf(fid,',%f',1);

fscanf(fid,'%s',1);
M.WLspan = fscanf(fid,'%f',1);

fscanf(fid,'%[^,]',1);
M.WLstart = fscanf(fid,',%f',1);

fscanf(fid,'%[^,]',1);
M.WLstop = fscanf(fid,',%f',1);

fgetl(fid);
fgetl(fid);
fgetl(fid);
fgetl(fid);

fscanf(fid,'%s',1);
M.WLres = fscanf(fid,'%f',1);

fscanf(fid,'%s',1);
M.WLavg = fscanf(fid,'%f',1);

fclose(fid);
```

```
end;
```

D.2 Data extraction from a PDL measurement file

```
% Filling of structure from PDL Measurement
function [M] = ReadMeasurementPDL(Filename)


fid = fopen(Filename,'r');

if (fid>0)
% reading of date and time
    fgetl(fid); fscanf(fid,'%s',1);
        M.date = fscanf(fid,'%s',1);

        fscanf(fid,'%s',1);
        M.time = fscanf(fid,'%s',1);

% reading of WL settings
        fscanf(fid,'%s',3);
        M.WLstart = fscanf(fid,'%f',1);

        fscanf(fid,'%s',2);
        M.WLstop = fscanf(fid,'%f',1);

        fscanf(fid,'%s',2);
        M.WLstep = fscanf(fid,'%f',1);

        fscanf(fid,'%s',2);
        M.WLpoints = fscanf(fid,'%f',1);

% reading of PDL results
        fscanf(fid,'%s',3);
        M.PDLmin = fscanf(fid,'%s',1);

        fscanf(fid,'%s',2);
        M.PDLmax = fscanf(fid,'%f',1);

        fscanf(fid,'%s',2);
        M.PDLavg = fscanf(fid,'%f',1);

% reading of recorded points
        fscanf(fid,'%s',4);
        M.data = fscanf(fid,'%f  ',[2,M.WLpoints]);

fclose(fid);

end;
```

D.3 Data extraction from a PMD measurement file

```
% Filling of structure from PMD Measurement
```

```
function [M] = ReadMeasurementPMD(Filename)


fid = fopen(Filename,'r');

if (fid>0)
% reading of date and time
    fgetl(fid); fscanf(fid,'%s',1);
        M.date = fscanf(fid,'%s',1);

        fscanf(fid,'%s',1);
    M.time = fscanf(fid,'%s',1);

% reading Fibre length
        fscanf(fid,'%s',3);
        M.length = fscanf(fid,'%f',1);

% reading of WL settings
        fscanf(fid,'%s',3);
        M.WLstart = fscanf(fid,'%f',1);

        fscanf(fid,'%s',2);
        M.WLstop = fscanf(fid,'%f',1);

        fscanf(fid,'%s',2);
        M.WLstep = fscanf(fid,'%f',1);

        fscanf(fid,'%s',2);
        M.WLpoints = fscanf(fid,'%f',1);

% reading of PMD results
        fscanf(fid,'%s',3);
        M.PMDmin = fscanf(fid,'%f',1);

        fscanf(fid,'%s',2);
        M.PMDmax = fscanf(fid,'%f',1);

        fscanf(fid,'%s',2);
        M.PMDavg = fscanf(fid,'%f',1);

        fscanf(fid,'%s',2);
        M.PMDrms = fscanf(fid,'%f',1);

        fscanf(fid,'%s',2);
        M.PMDskm = fscanf(fid,'%f',1);

% reading of recorded points
        fscanf(fid,'%s',8);
        M.data = fscanf(fid,'%f ,',[5,M.WLpoints]);

fclose(fid);

end;
```

D.4 Calcul of the coupling length regime

```
clear; close all;

Filename = '../../Curves/PMD/PaDo_A1_070605.pmd';
PMD_1 = ReadMeasurementPMD(Filename);
...

for i=1:1:10

var_data_2 = strcat('PMD_',num2str(i),'.data(2,:)');
var_PMDavg = strcat('PMD_',num2str(i),'.PMDavg');

%computation of extremum
[xmax,imax,xmin,imin] = extrema(PMD_1.data(2,:));

%computation of PMDavg crossing
[ci,ti] = crossings(eval(var_data_2),[],eval(var_PMDavg));

%computation of ratio
ratio(i) = (length(xmax)+length(xmin))/length(ci);

end
```

Appendix E

PaDo and *PaDowH* SEM pictures

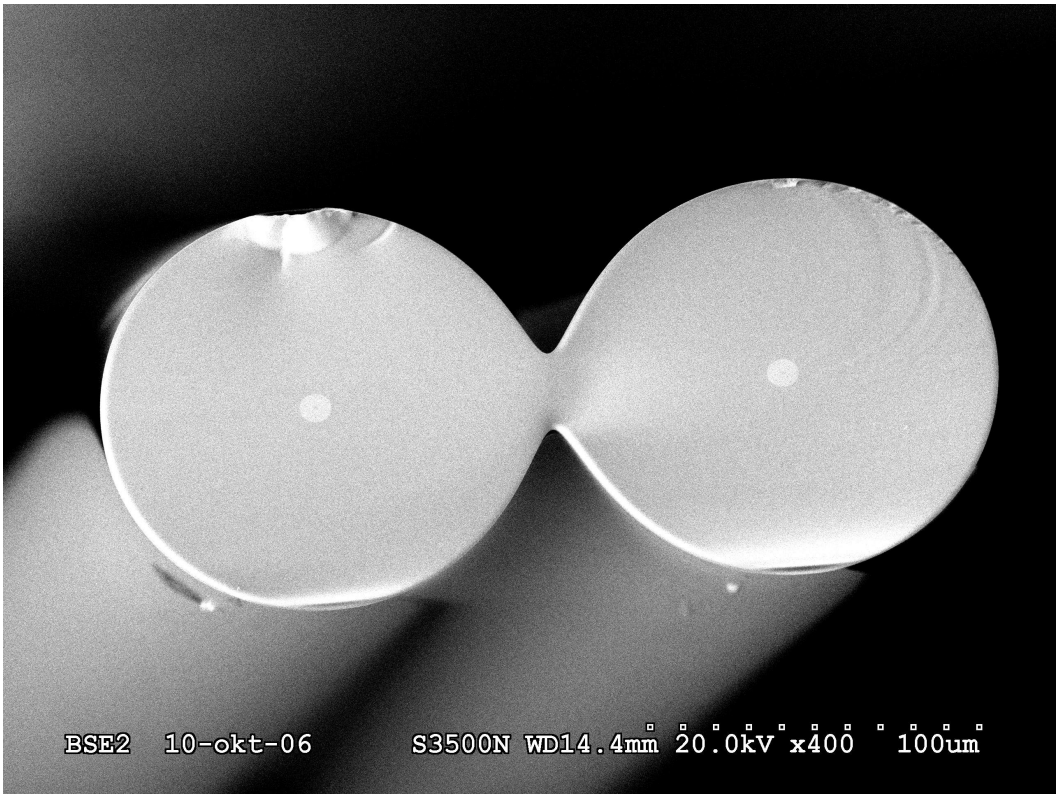

Figure E.1: Picture of a *PaDo* under a SEM

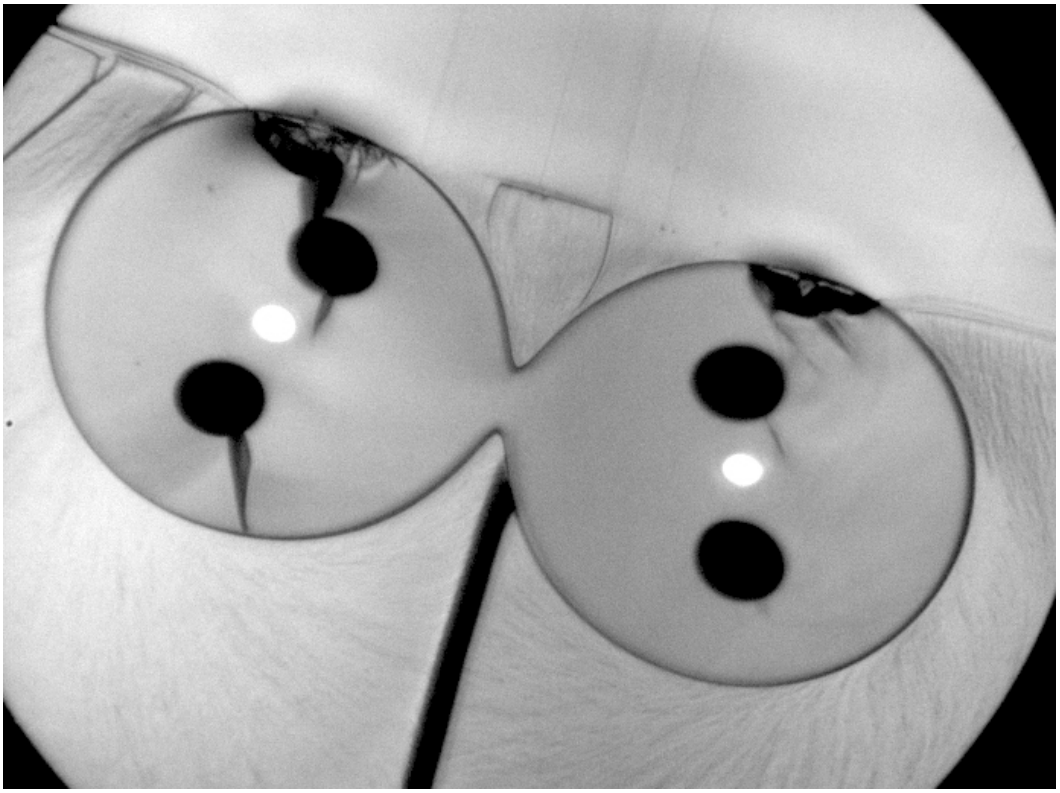

Figure E.2: Picture of a *PaDowH* under a SEM

Appendix F

Miscellenous pictures

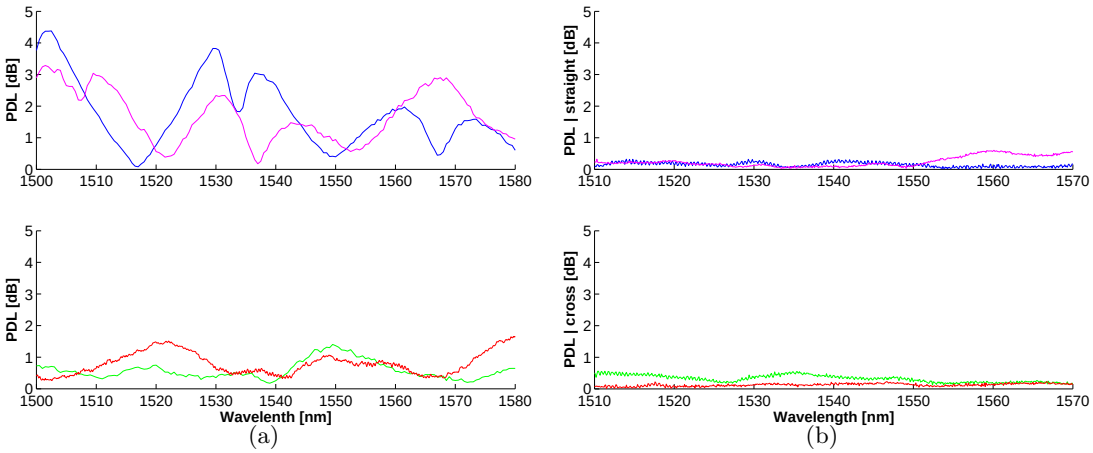

(a) (b)

Figure F.1: PDL of *Coupler A* (a) and *Coupler B* (b), straight arms at the top and cross arms at the bottom

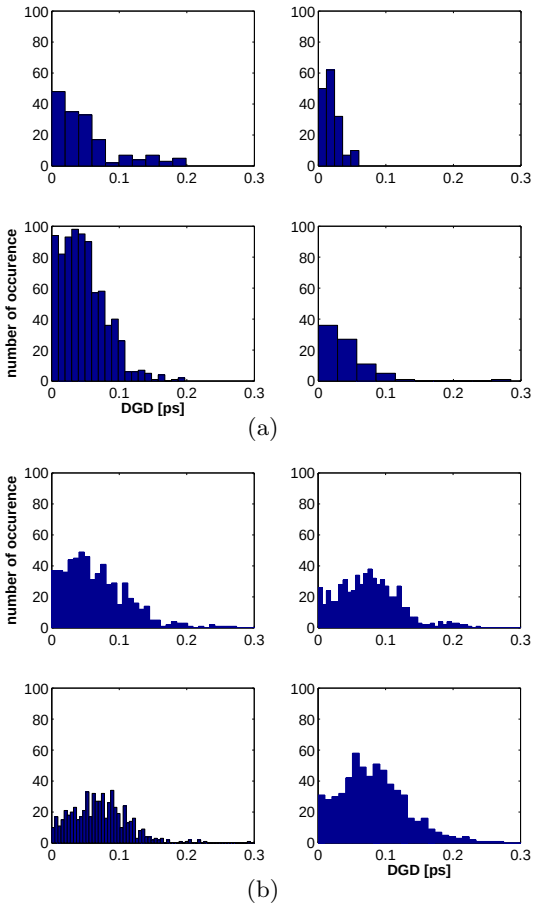

Figure F.2: DGD of *Coupler A* (a) and *Coupler B* (b), straight arms at the top and cross arms at the bottom